JGR Earth Surface

RESEARCH ARTICLE
10.1029/2021JF006266

Morphodynamic Equilibria in Double-Inlet Systems: Existence and Stability

X. Deng[1], C. Meerman[2], T. Boelens[3], T. De Mulder[3], P. Salles[4], and H. M. Schuttelaars[1]

[1]Department of Applied Mathematics, Delft University of Technology, Delft, The Netherlands, [2]Mathematical Institute, Leiden University, Leiden, The Netherlands, [3]Hydraulics Laboratory, Department of Civil Engineering, Ghent University, Ghent, Belgium, [4]Instituto de Ingenieria, Universidad Nacional Autónoma de México, Sisal, Mexico

Key Points:

- A cross-sectionally averaged morphodynamic model has been developed to assess equilibria of double-inlet systems at tidal barrier coasts
- No equilibrium, one equilibrium or multiple stable equilibria may exist, depending on the forcing conditions
- For a good comparison with the Marsdiep-Vlie system, inclusion of the basin's width variation is essential

Supporting Information:

Supporting Information may be found in the online version of this article.

Correspondence to:

X. Deng,
dengxiaosp@gmail.com

Citation:

Deng, X., Meerman, C., Boelens, T., De Mulder, T., Salles, P., & Schuttelaars, H. M. (2021). Morphodynamic equilibria in double-inlet systems: Existence and stability. *Journal of Geophysical Research: Earth Surface*, *126*, e2021JF006266. https://doi.org/10.1029/2021JF006266

Received 20 MAY 2021
Accepted 12 NOV 2021

Abstract The existence of morphodynamic equilibria of double-inlet systems is investigated using a cross-sectionally averaged morphodynamic model. The number of possible equilibria and their stability strongly depend on the forcing conditions and geometry considered. This is illustrated by considering a rectangular double-inlet system forced by M_2 tidal constituents only. Depending on the M_2 amplitudes and phases at both entrances, no equilibrium, one equilibrium or multiple morphodynamic equilibria may exist. In case no equilibrium is found, the minimum water depth becomes zero somewhere in the system, reducing the double-inlet system to two single-inlet systems. In the other cases, the location of the minimum water depth and the direction of the tidally-averaged sediment transport, as well as their actual values, depend strongly on the M_2 tidal characteristics. Such parameter sensitivity is also observed when including the residual and M_4 forcing contributions to the water motion, and when allowing for width variations. This suggests that, when considering a specific system, the number and stability of morphodynamic equilibria, as well as the characteristics of these quantities, can only be assessed by investigating that specific system in detail. As an example, the Marsdiep-Vlie inlet system in the Dutch Wadden Sea is considered. It is found that, by using parameter values and a geometry characteristic for this system, the water motion and bathymetry in morphodynamic equilibrium are qualitatively reproduced. Also the direction and order of magnitude of the tidally-averaged suspended sediment transport compare well with those obtained from a high-complexity numerical model.

Plain Language Summary An idealized model is developed to systematically investigate the cross-sectionally averaged morphodynamic equilibria in double-inlet systems with varying width. A bathymetric profile is in equilibrium with the water motion and sediment transport, if there is no accumulation of tidally averaged sediment transport, associated with the equilibrium bed. Considering a constant-width system, the number of morphodynamic equilibria strongly depends on the tidal forcings. For an M2 tidal forcing only, it is found that no equilibrium, one equilibrium or more than one morphodynamic equilibria can exist. The location and the depth of the watershed, and the total sediment transport are used to characterize the morphodynamic equilibria. Typically, the watershed tends to get closer to the inlet with a larger tidal amplitude, and the total transport is directed from the inlet with the largest tidal amplitude to the one with the smallest tidal amplitude. Taking parameter values representative of the Marsdiep-Vlie system, one stable morphodynamic equilibrium is found. Inclusion of the large-scale width variations observed in the Marsdiep-Vlie system is essential to obtain an equilibrium profile that qualitatively reproduces the observed width-averaged bathymetry, water motion and tidally-averaged sediment transport.

1. Introduction

A large part of the world's coastline can be characterized as barrier coasts (Mulhern et al., 2017), consisting of barrier islands, back-barrier basins and tidal inlets connecting the back-barrier basins to the open sea (de Swart & Zimmerman, 2009), with shape and size varying significantly from location to location (Glaeser, 1978; Stutz & Pilkey, 2011). Barrier coasts are highly dynamic, in part due to the complex nonlinear interactions among water motion, sediment transport and morphological evolution, as well as to their sensitivity to changes in external conditions caused, for example, by increased storm frequency and intensity, sea level rise and human interference (McBride et al., 1995; van der Spek, 1997). They are very important from an ecological and economical point of view. Their ecological value lies in their function as breeding and feeding grounds for aquatic and terrestrial species, their biodiversity and other ecosystem services they provide. Economical activities such as gas-mining,

Figure 1. Satellite image showing the bathymetry of the part of the Dutch Wadden Sea that contains the Marsdiep, Eijerlandse Gat and Vlie inlet systems (Copyright © USGS/ESA).

dredging and recreation are common in these regions. Furthermore, they are of importance for coastal safety (Glaeser, 1978).

An example of a barrier coast, where the back-barrier basin is connected to the open sea by multiple inlets, is the Wadden Sea along the Dutch, German and Danish coast (Oost et al., 2012). In Figure 1 a part of the Dutch Wadden Sea is shown as an example of such a system. Even though it is often assumed that the various inlets drain different sub-basins, separated from each other by a tidal watershed, recent studies have revealed a strong exchange of water (Duran-Matute et al., 2014) and sediment (Sassi et al., 2015) between adjacent sub-basins. Such interactions are also found in the Ria Formosa in south Portugal (Pacheco et al., 2008; Salles et al., 2005) and Venice Lagoon (Seminara et al., 2005; Tambroni & Seminara, 2006). This strongly suggests that to understand, model and predict the morphodynamic evolution of these systems, the interactions between sub-systems have to be taken into account, that is, these systems should be considered as multiple inlet systems. This is also necessary for long-term analysis, as observations show that these multiple inlet systems have been present for centuries.

To study the long-term morphodynamic stability of multiple inlet systems, van de Kreeke (1985, 1990a, 1990b) extended the single-inlet stability concept of Escoffier (1940) to multiple inlets. In his approach only the inlets are morphodynamically active, that is, the bathymetry in the back-barrier basin is fixed. Furthermore, he assumed that the water level in the back-barrier basin could be approximated as spatially uniform (pumping mode). He showed for double-inlet systems, and speculated for multiple inlet systems, that ultimately only one inlet would remain open. Because this contradicted long-term observations, van de Kreeke et al. (2008) extended the physics in the previous models by allowing for spatial variations in the free surface elevation in the back-barrier basin. This resulted in stable double-inlet systems, a finding confirmed in studies by Brouwer et al. (2012) and de Swart and Volp (2012) for double-inlet systems and Roos et al. (2013) and Reef et al. (2020) for multiple inlet systems.

One of the great advantages of these semi-empirical models is their computational efficiency, allowing for extensive sensitivity analysis of parameters such as tidal range, phase difference of the tidal forcing at the inlets and basin geometry, factors that strongly influence the morphodynamic stability of the inlet systems. However, these models do not allow the morphodynamic evolution of the back-barrier basin, even though observations and model studies show these regions to be morphodynamically active. For example, Dastgheib et al. (2008) used a high-complexity numerical model to simulate the long-term sediment transport and bottom evolution for a double-inlet system, resulting in the development of channel-shoal systems in the back-barrier basin. After simulating 2,000 years, the system was assumed to be close to a morphodynamic equilibrium with both inlets still open. A detailed analysis of the physical mechanisms resulting in the observed morphodynamic equilibrium is challenging using high-complexity numerical models, as it allows one to gain insight into the sensitivity of the morphodynamic equilibria to variations in parameters and geometric characteristics.

The aim of the present study is therefore to develop a process-based model for double-inlet system on mesotidal barrier coasts (Hayes, 1979) in which both the tidal inlets and back-barrier basin are morphodynamically active. The model will be used to analyze the existence of morphodynamic equilibria, their stability, and sensitivity to parameters and geometry. It should allow for a systematic analysis of the physical mechanisms leading to these morphodynamic equilibria. Motivated by the insights gained from width-averaged equilibrium models for single-inlet systems (Meerman et al., 2019; Schuttelaars & de Swart, 1996; Schuttelaars & de Swart, 2000; ter Brake & Schuttelaars, 2010), this type of models will be extended to allow for two tidal inlets connected to each other by a back-barrier basin of arbitrary length and width. Default parameters used are characteristic for a double-inlet system in the Dutch Wadden Sea, and results will be compared with observations and numerical model results from the Marsdiep-Vlie system. The existence and sensitivity of morphodynamic equilibria to geometry and forcing conditions off the seaward sides of the two inlets, consisting of M_2 and M_4 tidal constituents and a subtidal signal, will be investigated in detail.

In Section 2, the equations governing water motion, transport of sediment and bed evolution are presented. The scaling of the system of equations and the solution method are presented in Section 3. In Section 4, morphodynamic equilibria in double-inlet systems and their linear stability are studied. In Section 5, the results are discussed and in Section 6 conclusions are presented.

2. Model Description

The geometry under consideration is that of a tidal inlet system that is connected to the open sea by two inlets (for a top view see Figure 2b, which is obtained using the observed geometry in Figure 2a). The x axis in Figure 2b represents the distance along the centerline indicated in Figure 2a, whereas the y axis represents the distances normal to the centerline. The inlet system is aligned with the horizontal x axis, and has a prescribed length L. The basin is connected to the open sea at $x = 0$ and $x = L$, respectively. The width is allowed to vary with the longitudinal coordinate, and is denoted by $B(x) = B_2(x) - B_1(x)$, with B_2 and B_1 indicating the left and right coastal boundaries, looking from inlet I to inlet II. These coastal boundaries are assumed to be non-erodible. The width of inlet I is denoted by $B^I = B\,(0)$, and the width at inlet II by $B^{II} = B(L)$.

The undisturbed water depth at inlet I is denoted by H^I, and at $x = L$ by H^{II} (see Figure 2c for a side view). The free surface is represented by $z = \hat{\zeta}$, with the undisturbed free surface located at $z = 0$. The erodible bottom, that is assumed to consist of sandy material with a single grain size, is described by the equation $z = \hat{h} - H^I$, where H^I is used as the reference depth and $\hat{h}$ is the local bed elevation measured from level identified by the reference depth. Hence the instantaneous local water depth is given by $H^I - \hat{h} + \hat{\zeta}$.

Since, both the length and width of the inlet system are much larger than the reference water depth, and the width is much smaller than the basin length and the Rossby deformation radius, the water motion can be described by the cross-sectionally averaged equations for a homogeneous fluid (Csanady, 1982):

$$B\zeta_t + [B(H^I - h + \zeta)u]_x = 0, \tag{1a}$$

$$u_t + uu_x + g\zeta_x + \frac{r_* u}{H^I - h + \zeta} = 0. \tag{1b}$$

Here, ζ denotes the width-averaged sea surface elevation, defined as,

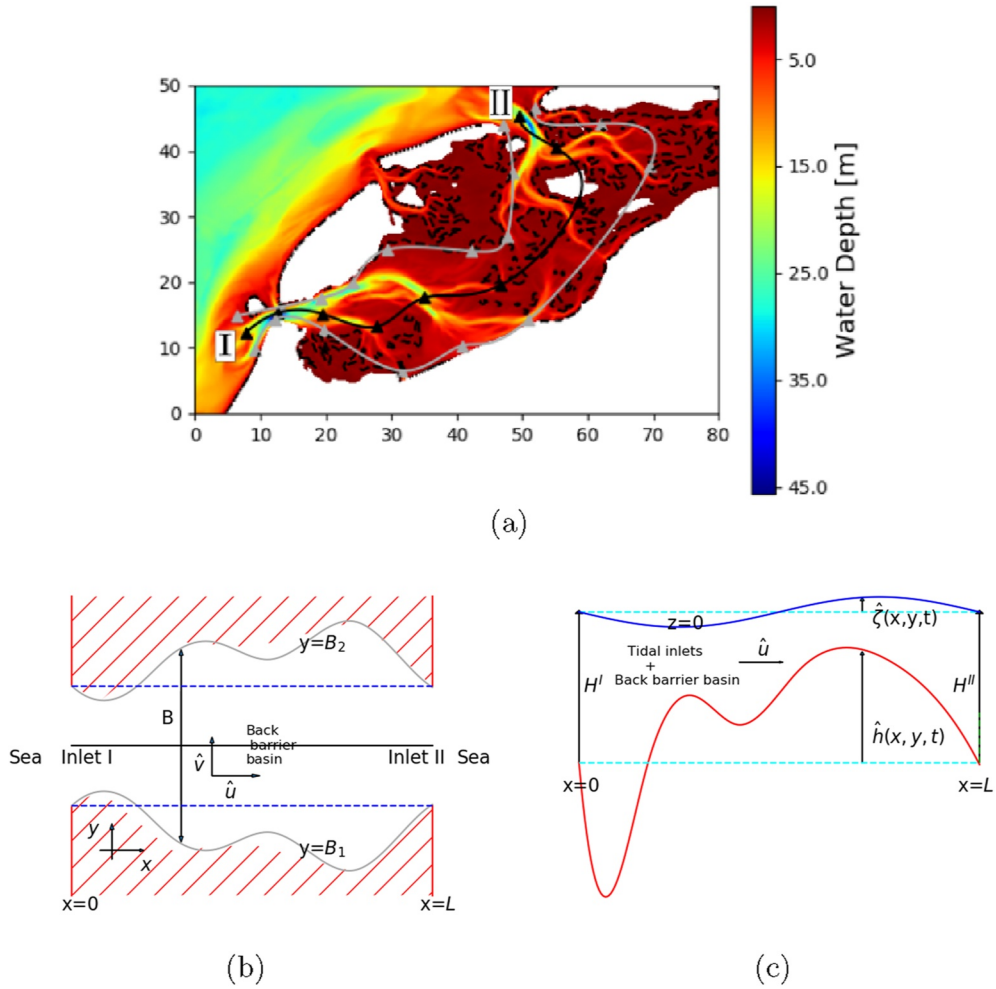

Figure 2. A sketch of the tidal embayment connected to the open sea at both ends. (a) The bathymetry in the Marsdiep-Vlie inlet system. The dark-gray solid lines indicate the coastal boundaries used in the model, whereas the centerline is indicated by a black solid line. For a more elaborate discussion, see Section 5.2. (b) A top view of the schematized double-inlet system with a varying width (dark-gray solid lines) and a uniform width (dashed blue lines). The longitudinal and lateral velocities are denoted by $\hat{u}$ and $\hat{v}$. (c) A cross-sectional view of the double-inlet system, with the depth at inlet I denoted by H^I and the depth at inlet II denoted by H^{II}. The bed profile (red line) is denoted by $\hat{h}(x, y, t)$, and the free surface elevation (blue line) by $\hat{\zeta}(x, y, t)$.

$$\zeta(x,t) = \frac{1}{B_2 - B_1} \int_{B_1}^{B_2} \hat{\zeta}(x,y,t) dy. \tag{2}$$

Similarly, $u\,(x, t)$ denotes the width-averaged horizontal longitudinal velocity and h the width-averaged bed level. Time is denoted by t, and g denotes the gravitational acceleration. Subscripts denote a derivative with respect to that variable. Following Lorentz (1922) and Zimmerman (1992), a linearized formulation of the friction is used with the bottom friction coefficient defined as $r_* = 8Uc_d/3\pi$, with U a characteristic velocity scale and c_d a drag coefficient. The characteristic velocity U will be introduced in Section 3.1.

The variables ζ and u can be decomposed in a residual and a time-varying contribution as $\zeta = <\zeta> + \bar{\zeta}$ and $u = <u> + \bar{u}$, where $<\cdot>$ denotes tidal averaging, and $\bar{\cdot}$ the deviation from the tidal average, such that $<\bar{\cdot}> = 0$. The time dependent sea surface elevations at the two inlets are prescribed as,

$$\bar{\zeta} = A^I_{M_2} \cos(\sigma t - \phi^I_{M_2}) + A^I_{M_4} \cos(2\sigma t - \phi^I_{M_4}) \quad \text{at} \quad x = 0, \tag{3a}$$

$$\bar{\zeta} = A^{II}_{M_2} \cos(\sigma t - \phi^{II}_{M_2}) + A^{II}_{M_4} \cos(2\sigma t - \phi^{II}_{M_4}) \quad \text{at} \quad x = L. \tag{3b}$$

It should be noted that, when considering the morphodynamic *evolution* of a tidal basin, the effect of radiation damping on the tidal forcing at the seaward side can only be neglected in the so-called *deep sea limit* (Roos & Schuttelaars, 2015). However, if one is only interested in morphodynamic equilibria, prescribing the tidal forcing is allowed. One should interpret the morphodynamic equilibria as obtained for that prescribed tidal forcing. For the tidally-averaged hydrodynamic components, we require

$$<\zeta> = 0 \text{ at } x = 0, \tag{4a}$$

$$<B(H - h - \zeta)u> = Q_* \text{ at } x = L. \tag{4b}$$

The constants $A^I_{M_2}$ ($A^I_{M_4}$) and $A^{II}_{M_2}$ ($A^{II}_{M_4}$) denote the amplitude of the M_2 (M_4) tide at the seaward sides of inlet I and II, respectively. Their corresponding phases are given by $\phi^I_{M_2}$ ($\phi^I_{M_4}$) and $\phi^{II}_{M_2}$ ($\phi^{II}_{M_4}$). The angular frequency of the M_2 tidal signal is given by $\sigma = 2\pi/T$, with T the M_2 tidal period. Condition (4a) implies that at the first inlet the tidally-averaged water depth is given by H^I, whereas the mean water depth at inlet II may deviate with respect to the undisturbed water level due to a mean difference in the mean sea surface elevation on the seaward side of the two inlets. The boundary condition (4b) at inlet II assumes the depth-averaged residual water transport equals Q_*. When Q_* is positive it represents a residual transport from inlet I to II, a negative value implies a net transport from inlet II to inlet I.

The sediment in the tidal inlet system consists of non-cohesive material with a uniform grain size of $2 \cdot 10^{-4}$ m. The sediment is mainly transported as suspended load, which is described by the width-averaged and depth-integrated concentration equation (ter Brake & Schuttelaars, 2010, 2011):

$$BC_t + \left[BuC - k_{h*}B\left(C_x + \frac{w_s}{k_{v*}}\beta h_x C\right)\right]_x = B\left(\alpha u^2 - \frac{w_s^2}{k_{v*}}\beta C\right), \tag{5}$$

where C is the depth-integrated and width-averaged suspended sediment concentration, k_{h*} is the horizontal diffusivity, k_{v*} is the vertical diffusivity, w_s is the settling velocity, α is the erosion parameter (Dyer, 1986) related to sediment properties, and β is the deposition parameter, defined by ter Brake and Schuttelaars (2010) for details.

$$\beta = \frac{1}{1 - \exp\left(-\frac{w_s}{k_{v*}}(H^I - h + \zeta)\right)}. \tag{6}$$

The tidally-averaged erosion and deposition are assumed to balance each other at seaward entrances, and it is assumed that no diffusive boundary layers develop at these locations in the time-dependent parts of the sediment concentration (Schuttelaars & de Swart, 2000). The resulting boundary conditions read:

$$<\alpha u^2 - \frac{w_s^2}{k_{v*}}\beta C> = 0 \text{ at } x = 0 \text{ and } L, \tag{7a}$$

$$\lim_{k_{h*}\to 0} \bar{C}(x, t, k_{h*}) = \bar{C}(x, t, k_{h*} = 0) \text{ at } x = 0 \text{ and } L. \tag{7b}$$

The width-averaged bed evolution equation is derived from the mass balance in the sediment layer and reads:

$$B\rho_s(1 - p)h_t = -B\left(\alpha u^2 - \frac{w_s^2}{k_{v*}}\beta C\right). \tag{8}$$

Here, ρ_s is the density of the sediment and p denotes the bed porosity. The first and second term on the right of Equation 8 model the local erosion and deposition of sediment, respectively.

Substituting Equation 5 into Equation 8 results in the following bed evolution equation:

$$B[\rho_s(1 - p)h_t + C_t] = -F_x, \tag{9}$$

with

$$F = \underbrace{-k_{h*}BC_x}_{F_{\text{diff}}} + \underbrace{-k_{h*}\frac{w_s}{k_{v*}}B\beta h_x C}_{F_{\text{topo}}} + \underbrace{BuC}_{F_{\text{adv}}}, \tag{10}$$

Table 1
Relevant Variables Adopted in the Model. Characteristic Values Are Those Estimated for the Marsdiep-Vlie Inlet System by Ridderinkhof (1988) and Duran-Matute et al. (2014)

System	Sediment	Bed
$L = 59$ km	$k_{h^*} = 10^2$ m^2 s^{-1}	$\rho_s = 2{,}650$ kg m^{-3}
$g = 9.81$ m s^{-2}	$\alpha = 0.5 \cdot 10^{-2}$ kg s m^{-4}	$p = 0.4$
$c_d = 0.0025$	$w_s = 0.015$ m s^{-1}	
$\sigma = 1.4 \cdot 10^{-4}$ s^{-1}	$k_{v^*} = 0.1$ m^2 s^{-1}	
$T = 44.9 \cdot 10^3$ s	$d_{50} = 2 \cdot 10^{-4}$ m	
$Q_* = -900$ m^{3}s^{-1}		
Marsdiep inlet	Vlie inlet	
$H^I = 11.7$ m	$H^{II} = 11.9$ m	
$A^I_{M_2} = 0.62$ m	$A^{II}_{M_2} = 0.77$ m	
$\phi^I_{M_2} = 148°$	$\phi^{II}_{M_2} = -158°$	
$B^I = 5{,}954$ m	$B^{II} = 5{,}619$ m	
$A^I_{M_4} = 0.11$ m	$A^{II}_{M_4} = 0.06$ m	
$\phi^I_{M_4} = 155°$	$\phi^{II}_{M_4} = -121°$	

the total depth-integrated and width-averaged sediment transport. This transport consists of three terms: a diffusive contribution related to the diffusion of depth-integrated concentration (F_{diff}), a diffusive contribution related to topographical variations (F_{topo}) and an advective contribution (F_{adv}).

At both boundaries, we prescribe the undisturbed bed level as,

$$h = 0 \text{ at } x = 0, \tag{11a}$$

$$h = H^I - H^{II} \text{ at } x = L. \tag{11b}$$

Since, erosion and deposition are assumed to balance each other at both entrances (see Equation 7), the undisturbed water depth at the entrances will not change during a morphodynamic experiment. The focus of this paper is on morphodynamic equilibria and not the evolution toward these equilibria. Hence, these boundary conditions are appropriate to obtain morphodynamic equilibria characterized by the specific depths prescribed at the seaward sides of the inlet (see also Schuttelaars and de Swart (1996, 2000) for a discussion of boundary conditions in a single inlet system). When considering the morphodynamic evolution in time of tidal inlet systems, instead of focusing on morphodynamic equilibria, these boundary conditions are too restrictive and more dynamic ones have to be used (see e.g., Bolla Pittaluga et al., 2014; Lanzoni & Seminara, 2002).

3. Solution Method

3.1. Scaling and Expansion

To make the equations dimensionless, the physical variables are scaled as,

$$x = L\check{x}, t = \sigma^{-1}\check{t}, u = U\check{u}, \tag{12a}$$

$$\zeta = A^I_{M_2}\check{\zeta}, h = H^I\check{h}, C = \frac{\alpha U^2 k_{v*}}{w_s^2}\check{C}, \quad B = B^I\check{B}, \tag{12b}$$

where the dimensionless variables are indicated by $\check{}$. For the horizontal coordinate x, the length L of the double-inlet system is the appropriate scale as the focus is on basin scale dynamics. The width is made dimensionless using the width at inlet I, B^I. Time is made dimensionless using the M_2 angular frequency σ, the surface elevation using the M_2 amplitude at the seaward side of inlet I, denoted by $A^I_{M_2}$, and the bed level is made dimensionless using the depth H^I at inlet I. The typical scale for the velocity is $U = A^I_{M_2}\sigma L/H^I$. It is obtained by assuming that the amplitude of the sea surface elevation at the first inlet is nonzero, otherwise the amplitude at the seaward side of the second inlet should be used (see details in Text S1 in Supporting Information S1). The suspended sediment concentration is made dimensionless using $\alpha U^2 k_{v*}/w_s^2$, which follows from assuming an approximate balance between erosion and deposition. In Table 1, characteristic values of the relevant parameters are given for the Marsdiep-Vlie system.

Substituting these dimensionless variables in the equations and suppressing the checks $\check{}$, the system of dimensionless equations reads:

$$B\zeta_t + [B(1 - h + \epsilon\zeta)u]_x = 0, \tag{13a}$$

$$u_t + \epsilon u u_x + \lambda_L^{-2}\zeta_x + \frac{ru}{1 - h + \epsilon\zeta} = 0, \tag{13b}$$

$$a[BC_t + (B\epsilon uC - k_h BC_x - k_h\lambda_d B\beta h_x C)_x] = B(u^2 - \beta C), \tag{13c}$$

$$B(h_t + a\delta_s C_t) = \delta_s B\left[ak_h C_x + ak_h\lambda_d\beta h_x C - a\epsilon uC\right]_x, \tag{13d}$$

with the dimensionless deposition parameter β given by,

Table 2
The Definition of Dimensionless Parameters and Their Values for the Marsdiep-Vlie System

Parameter	Definition	Value	Parameter	Definition	Value
ϵ	$\frac{A^I_{M_2}}{H^I} = \frac{U}{\sigma L}$	$5.30 \cdot 10^{-2}$	λ_L	$\frac{\sigma L}{\sqrt{H^I g}}$	0.77
R	$\frac{r_*}{H^I \sigma}$	$5.67 \cdot 10^{-1}$	a	$\frac{k_{v*}\sigma}{w_s^2}$	$6.22 \cdot 10^{-2}$
k_h	$\frac{k_{h*}}{L^2\sigma}$	$2.05 \cdot 10^{-4}$	δ_s	$\frac{\alpha U^2}{\rho_s(1-p)H^I\sigma}$	$3.68 \cdot 10^{-4}$
Q	$\frac{Q_*}{B^I H^I U}$	$-2.95 \cdot 10^{-2}$	λ_d	$\frac{H^I w_s}{k_{v*}}$	1.75
Γ	$\frac{A^I_{M_4}}{A^I_{M_2}}$	$1.83 \cdot 10^{-1}$	A^{II}_{r2}	$\frac{A^{II}_{M_2}}{A^I_{M_2}}$	1.25
A^{II}_{r4}	$\frac{A^{II}_{M_4}}{A^I_{M_4}}$	0.535	ϕ^{II}_{r2}	$\phi^{II}_{M_2} - \phi^I_{M_2}$	54°
ϕ^I_{r4}	$\phi^I_{M_4} - 2\phi^I_{M_2}$	− 141°	ϕ^{II}_{r4}	$\phi^{II}_{M_4} - 2\phi^I_{M_2}$	−57°

$$\beta = \frac{1}{1 - \exp(-\lambda_d(1 - h + \epsilon\zeta))}. \tag{14}$$

The parameter $\epsilon = A^I_{M_2}/H^I$ is the ratio of the M_2 tidal amplitude to the water depth at inlet I. In many tidal inlet systems $\epsilon \sim 0.1$, indicating that ϵ is a small parameter. Hereafter, it is assumed that $\epsilon\zeta$ is always much smaller than the local undisturbed water depth $1 - h$, thus neglecting the effects of drying and flooding. Note that ϵ is also equal to the ratio of the tidal excursion length and the length of the tidal inlet system $U\sigma/L$. The parameter $\lambda_L = k_g L$ is the product of the frictionless tidal wavenumber $k_g = \sigma/\sqrt{H^I g}$ to the length of the inlet system. The dimensionless friction parameter is denoted by r and is defined as $r = r_*/H^I\sigma$. The ratio of the deposition timescale to the tidal period is denoted by $a = k_{v*}\sigma/w_s^2$, and the sediment Péclet number $\lambda_d = H^I w_s/k_{v*}$ is the ratio of the typical time it takes for a particle to be mixed through the water column to the typical time it takes to settle in the water column. The parameter $\delta_s = \alpha U^2/(\rho(1-p)H^I\sigma)$ denotes the ratio of tidal period T to the time scale related to suspended load and is typically small. All dimensionless parameters and the assigned values are summarized in Table 2.

The bed evolution Equation 13d shows that at the tidal timescale the bed changes are very small, namely of $O(\delta_s)$. This implies that the bed changes significantly at a much larger time scale, the so-called morphodynamic time scale, defined as $\tau = \delta_s t$. To distinguish between these time scales, a multiple timescale method is used, with t the short tidal time variable and τ the long morphodynamic time variable. Using this multiple timescale approximation, it can be demonstrated that at the leading order of approximation the bed changes are due to tidally-averaged convergences and divergences of sediment (see Krol, 1991; Sanders & Verhulst, 1985). The resulting tidally-averaged bed evolution equation reads,

$$Bh_\tau = <-F>_x,$$

$$\text{with} \qquad F = \underbrace{-ak_h BC_x}_{F_{\text{diff}}} + \underbrace{-ak_h\lambda_d B\beta h_x C}_{F_{\text{topo}}} + \underbrace{a\epsilon BuC}_{F_{\text{adv}}}. \tag{15}$$

The dimensionless boundary conditions associated to Equations 13 and 15 read:

$$\zeta = \cos t + \gamma\cos(2t - \phi^I_{r4}) \quad \text{at} \quad x = 0, \tag{16a}$$

$$\zeta = A^{II}_{r2}\cos(t - \phi^{II}_{r2}) + \gamma A^{II}_{r4}\cos(2t - \phi^{II}_{r4}) \quad \text{at} \quad x = 1, \tag{16b}$$

$$<\zeta> = 0 \quad \text{at} \quad x = 0, \tag{16c}$$

$$<B(1 - h + \epsilon\zeta)u> = Q \quad \text{at} \quad x = 1, \tag{16d}$$

$$<u^2 - \beta C> = 0 \quad \text{at} \quad x = 0, 1, \tag{16e}$$

$$\lim_{k_h \to 0} \bar{C}(x, t, k_h) = \bar{C}(x, t, k_h = 0) \quad \text{at} \quad x = 0, 1. \tag{16f}$$

The parameter γ is the ratio of the amplitude of the M_4 tide and M_2 tide at inlet I, and $A^{II}_{r2} = A^{II}_{M_2}/A^{I}_{M_2}$ ($A^{II}_{r4} = A^{II}_{M_4}/A^{I}_{M_4}$) is the ratio of the amplitude of the M_2 (M_4) tide at inlet II and at inlet I. Parameter $\phi^{II}_{r2} = \phi^{II}_{M2} - \phi^{I}_{M2}$ ($\phi^{I}_{r4} = \phi^{I}_{M4} - 2\phi^{I}_{M2}$, $\phi^{II}_{r4} = \phi^{II}_{M4} - 2\phi^{I}_{M2}$) is the phase difference between the M_2 tide at inlet II (the M_4 tide at inlet I, the M_4 tide at inlet II) and M_2 tide at inlet I. $Q = Q_*/(B^I H^I U)$ is the dimensionless residual water transport.

In most tidal inlet systems, the parameters ϵ and γ are much smaller than 1 (see Table 2), allowing for the introduction of an asymptotic expansion in ϵ and γ of the physical variables $\Phi \in \{\zeta, u, C\}$,

$$\Phi = \Phi^{00} + \epsilon\Phi^{10} + \gamma\Phi^{01} + \text{h.o.t.}, \tag{17}$$

where the first superscript denotes the order in ϵ while the second denotes the order in γ. Because the water motion is forced with a time-periodical signal, each physical variable can be decomposed as a (infinite) sum of tidal constituents and a residual component,

$$\Phi = \Phi_{\text{res}}(x) + \sum_{k=1}^{\infty} \Phi_{ck}(x) \cos kt + \sum_{k=1}^{\infty} \Phi_{sk}(x) \sin kt, \tag{18}$$

where the subscript "res" denotes the tidally-averaged contribution to the variable Φ, and the contributions that temporally vary as cosines (sines) with frequency k are denoted with the subscript ck (sk).

The system of Equations 13a, 13b, 13c, 15 and the boundary conditions (16) can first be ordered in terms of ϵ and γ, and then in terms of the tidal constituents.

To obtain the tidally-averaged contributions that include both the dominant advective and diffusive transport mechanisms, the system of Equations 13a, 13b, 13c and 15 has to be solved up to the orders $\mathcal{O}(\epsilon)$ and $\mathcal{O}(\gamma)$. Both the water motion and the suspended sediment concentration consist of a M_2 and a M_4 tidal constituent, and a residual component. This results in tidally-averaged sediment transport contributions due to diffusive and advective processes. The diffusive transport consists of the two contributions F^{00}_{diff} and F^{00}_{topo}. The advective transport can be decomposed in two contributions, denoted as F^{20}_{adv} and F^{11}_{adv} of order $\mathcal{O}(\epsilon^2)$ and $\mathcal{O}(\epsilon\gamma)$, respectively. The internally-generated advective transport F^{20}_{adv} is due to the temporal correlation of internally-generated overtides and residual velocities at $\mathcal{O}(\epsilon)$ with the leading order concentration fields, and the correlation of the leading order velocities with the $\mathcal{O}(\epsilon)$ concentration. The externally-generated advective transport F^{11}_{adv} results from the temporal correlation of externally-generated overtides with the leading order concentration fields, and the correlation of the leading order velocities with the $\mathcal{O}(\gamma)$ concentration. The resulting tidally-averaged sediment transport contributions are then given by,

$$<F^{00}_{\text{diff}}> = -ak_h B C^{00}_{\text{res},x}, \tag{19}$$

$$<F^{00}_{\text{topo}}> = -ak_h \beta \lambda_d B h_x C^{00}_{\text{res}}, \tag{20}$$

$$<F^{20}_{\text{adv}}> = \frac{1}{2} a\epsilon^2 B(u^{00}_{c1}C^{10}_{c1} + u^{00}_{s1}C^{10}_{s1} + 2u^{10}_{\text{res}}C^{00}_{\text{res}} + u^{10}_{c2}C^{00}_{c2} + u^{10}_{s2}C^{00}_{s2}), \tag{21}$$

$$<F^{11}_{\text{adv}}> = \frac{1}{2} a\epsilon\gamma B(u^{00}_{c1}C^{01}_{c1} + u^{00}_{s1}C^{01}_{s1} + u^{01}_{c2}C^{00}_{c2} + u^{01}_{s2}C^{00}_{s2}). \tag{22}$$

3.2. Morphodynamic Equilibria and Linear Stability

The resulting system of morphodynamic equations, ordered in terms of the small parameters and expanded in tidal constituents, can be written as,

$$K\boldsymbol{\Psi}_\tau = G(\boldsymbol{\Psi}, \mathbf{p}), \tag{23}$$

where $\mathbf{\Psi}$ is the vector of physical variables and $\mathbf{p}$ the vector of model parameters. The matrix K is a diagonal matrix, with a non-zero element only in the row associated with the bed evolution equation. The nonlinear operator G depends on the parameters $\mathbf{p}$ and works on the physical variables $\mathbf{\Psi}$.

To obtain solutions of this system of equations, Equation 23 is discretized using a finite element method with continuous Lagrange elements (Alnæs et al., 2015, see also Text S2.1 in Supporting Information S1). Adopting a weak formulation and using a Galerkin method (Brenner & Scott, 2002), the discretized system of equations reads,

$$\mathcal{K}\tilde{\Psi}_\tau = \mathcal{G}(\tilde{\Psi}, \mathbf{p}), \tag{24}$$

in which $\tilde{\Psi}$ is the discretization of $\mathbf{\Psi}$, $\mathcal{K}$ is the discretized matrix corresponding to K and $\mathcal{G}$ is the discretized nonlinear operator working on $\tilde{\Psi}$ and the parameters $\mathbf{p}$.

This discretized system of equations can be analyzed using two different approaches, the *initial value* and the *bifurcation* approach. The latter approach aims at the direct identification of morphodynamic equilibria, whereas with the former approach an initially prescribed bathymetry is integrated in time.

In this paper, the focus is on the bifurcation approach with which we directly solve for equilibrium states $\tilde{\Psi}_\mathrm{e}$ that satisfy,

$$\mathcal{G}(\tilde{\Psi}_\mathrm{e}, \mathbf{p}_0) = 0, \tag{25}$$

in which $\mathbf{p}_0$ is a vector of prescribed parameter values. To obtain the equilibrium solutions $\tilde{\Psi}_\mathrm{e}$, a Newton-Raphson iterative method is used. An initial guess $\tilde{\Psi}_\mathrm{i}$ of a morphodynamic equilibrium is updated iteratively until the corrections are small enough (in this study the iteration is stopped when the maximum correction is smaller than 10^{-8}).

For this iterative procedure to converge, the initial guess $\tilde{\Psi}_\mathrm{i}$ has to be close enough to the morphodynamic equilibrium associated with the parameter vector $\mathbf{p}_0$. If no information about an approximate morphodynamic equilibrium is available, a good initial guess can be obtained by integrating the discretized system (24) starting from an arbitrary initial bed profile in time (in this study a backward Euler method is used as time-integration method, see the Text S2.3 in Supporting Information S1 for details), until an approximate equilibrium is reached. This approximate equilibrium can then be used as the initial guess $\tilde{\Psi}_\mathrm{i}$ in the Newton-Raphson iterative procedure. If for a given parameter vector $\mathbf{p}_0$ a morphodynamic equilibrium is found, a so-called continuation method (Seydel, 1994) can be employed to find equilibria for different parameter values $\mathbf{p}_1$ by slowly changing the parameters from $\mathbf{p}_0$ to $\mathbf{p}_1$. During this continuation process, the previously obtained equilibrium is used as a first guess in the iteration process, resulting in the morphodynamic equilibrium for the new parameter vector $\mathbf{p}_1$. The continuation method employed in this paper is the arclength method (see Crisfield, 1981; Dijkstra et al., 2014; and the discussion in Text S2.2 in Supporting Information S1).

The linear stability of the morphodynamic equilibria $\tilde{\Psi}_e$ (corresponding to parameter $\mathbf{p}_e$) can be investigated by substituting $\tilde{\Psi} = \tilde{\Psi}_e + \Delta\tilde{\Psi}\exp(\omega\tau)$ into Equation 24 and linearizing the resulting equation. The resulting eigenvalue problem reads:

$$\omega\mathcal{K}\Delta\tilde{\Psi} = \mathcal{J}_\mathcal{G}(\tilde{\Psi}_e, \mathbf{p}_e)\Delta\tilde{\Psi}, \tag{26}$$

in which $\mathcal{J}_\mathcal{G}(\tilde{\Psi}_e, \mathbf{p}_e)$ is the Jacobian, ω the eigenvalue and $\Delta\tilde{\Psi}$ the associated eigenvector. An equilibrium is called linearly stable if all its eigenvalues have a negative real part, and unstable if at least one eigenvalue has a positive real part.

4. Results

In the numerical experiments presented in this section, the influence of the forcing conditions and geometry on morphodynamic equilibria is presented. Assuming a constant width, that is, a system with a rectangular planform, the morphodynamic equilibria are first obtained for a water motion forced by a M_2 tidal constituent and presented in Section 4.1. Next (Section 4.2), all hydrodynamic forcing contributions are included. Finally (Section 4.3), the

influence of width variations is investigated. All results are obtained using parameter values that are representative of the Marsdiep-Vlie inlet system (see Table 1), unless mentioned otherwise.

4.1. Constant-Width System Subjected to a M_2 Tidal Forcing

The influence of variations in the prescribed M_2 tidal constituent on the resulting morphodynamic equilibria has been studied by setting the amplitude and phase of the M_2 tide at inlet I equal to 0.62 m and 0° and varying the M_2 amplitude and phase at inlet II. To focus only on the influence of the M_2 forcing, the amplitudes of the externally prescribed overtides (A^I_{M4} and $A^{II}_{M_4}$) are assumed to be zero. Furthermore, the undisturbed water depths at both inlets are taken to be 11.7 m and the tidally-averaged water transport Q at the second inlet is set to zero. Sensitivity to inlet depth and tidally-averaged water transport at inlet II, assuming no M_4 tidal forcing, is discussed in the Text S3 in Supporting Information S1. All other parameter values are taken from Table 1.

The resulting morphodynamic equilibrium condition reads,

$$\frac{d}{dx}\left(<F^{00}_{\text{diff}}> + <F^{00}_{\text{topo}}> + <F^{20}_{\text{adv}}>\right) = 0, \tag{27}$$

where for the numerical experiment under consideration, the width within the inlet system is constant for all x, that is, $B(x) = B^I$.

To obtain these morphodynamic equilibria, the evolution of a spatially uniform bed is studied (i.e., the system of Equation 24 is integrated in time using a Backward-Euler method). If the divergence of the tidally-averaged sediment transport vanishes, an equilibrium is reached. Two numerical experiments have been carried out with different M_2 tidal forcings applied at the second inlet.

In the first numerical experiment, we take $A^{II}_{M_2} = 0.77$ m, $\phi^{II}_{M_2} = 54°$ (default value). The resulting bed evolution is shown in Figure 3a. After approximately 2,500 years, the bed profile reaches its equilibrium with a maximum water depth (WD_{max}) of 17.8 m, located at approximately 20 km from inlet I.

In the second numerical experiment, we take $A^{II}_{M_2} = 0.77$ m and $\phi^{II}_{M_2} = 0°$. The development of the bed profile for the first 23,200 years is shown in Figure 3b. This figure clearly shows that the water depth decreases over time, and after approximately 23,300 years, it vanishes near km 32. The two inlets are not connected anymore, and a system formed by two single inlets is eventually obtained.

From the previous two numerical experiments, it is evident that a morphodynamic equilibrium in which both inlets are connected does not necessarily exist for all combinations of $A^{II}_{M_2}$ and $\phi^{II}_{M_2}$. The minimum water depth, denoted by WD_{min}, can vanish at some location, disconnecting the two inlets. To assess the existence of morphodynamic equilibria with both inlets connected for a wider range of forcing conditions, we take $A^{II}_{M_2} = 0.77$ m, and vary $\phi^{II}_{M_2}$ from $-180°$ to 180°. Figure 3c shows the equilibrium water depth as a function of position along the embayment (horizontal axis) and the M_2 phase at inlet II (vertical axis). The equilibrium water depth is found to strongly depend on the tidal phase at inlet II. By increasing $\phi^{II}_{M_2}$ from $-180°$ to $-2°$, WD_{min} decreases from 11.7 to 2.5 m, and by decreasing $\phi^{II}_{M_2}$ from 180° to 13°, WD_{min} varies from 11.7 to 6.0 m. For a phase between $-2°$ and 13°, no double-inlet morphodynamic equilibrium exists.

To quickly characterize these morphodynamic equilibria, the quantities WD_{min} and its location will be used. As an example, using a constant amplitude $A^{II}_{M_2} = 0.77$ m, WD_{min} is shown as a function of $\phi^{II}_{M_2}$ in Figure 3d. Two distinct branches of morphodynamic equilibrium solutions are found, each consisting of a stable (solid) and unstable (dashed) part. The stable and unstable solutions on each branch are connected by a so-called limit points, denoted by $L1$ and $L2$. For phases with values between the two limit points, no equilibria were found with both inlets connected. Note that the stable solutions correspond to the equilibria shown in Figure 3c.

To be more precise, Figure 3d indicates that the number of morphodynamic equilibria and their stability strongly depends on the value of the phase at inlet II. For $-1.9° \leq \phi^{II}_{M_2} \leq 12.8°$ no morphodynamic equilibrium exists, for $-53° \leq \phi^{II}_{M_2} \leq -1.9°$ and $12.8° \leq \phi^{II}_{M_2} \leq 47°$ two morphodynamic equilibria (one stable and one unstable) exist, whereas for all other phase values one stable equilibrium exists. Furthermore, the number of morphodynamic equilibria and their stability not only depends on the phase of the M_2 tide at inlet II, but also on its amplitude. Figure 4 shows the number of morphodynamic equilibria as a function of the amplitude $A^{II}_{M_2}$ and the phase $\phi^{II}_{M_2}$.

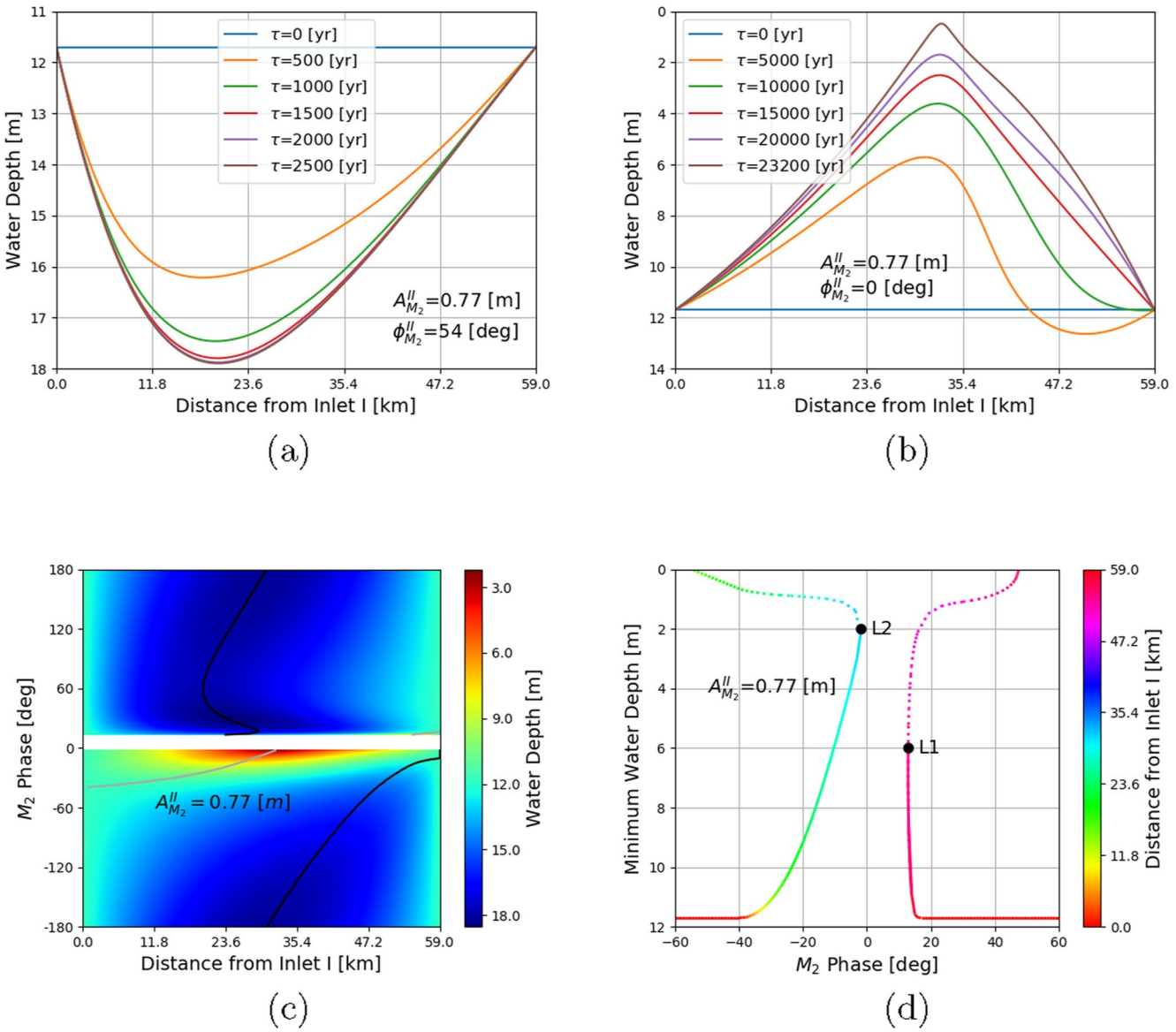

Figure 3. Bed evolution computed for a constant-width double-inlet system forced with a M_2 tide. In panel (a), the bed profile starts to evolve from an initial flat bottom. The temporal evolution is computed using the Backward-Euler time-integration method with $A^{II}_{M_2} = 0.77$ m and $\phi^{II}_{M_2} = 54°$, the unit of τ is year. Panel (b) shows the results of the numerical experiment as in panel (a), but with $A^{II}_{M_2} = 0.77$ m and $\phi^{II}_{M_2} = 0°$. Panel (c) shows equilibrium water depth for $A^{II}_{M_2} = 0.77$ m and $\phi^{II}_{M_2}$ varying from −180° to 180°, with colder colors denoting larger water depths and warmer colors smaller water depths. If no equilibrium is found, a white color code is used. The location of WD_{min} is indicated by gray contours and the location of the WD_{max} is indicated by black contours. Panel (d) shows WD_{min} of equilibrium bed profiles with $A^{II}_{M_2} = 0.77$ m and $\phi^{II}_{M_2}$ varying from −60° to 60°. The color indicates the distance of the WD_{min} from inlet I, with warmer colors closer to (one of) the entrance(s), and colder colors more toward the middle of the channel. Morphodynamic equilibria that are linearly stable are indicated by a solid line, while those indicated by a dashed line are linearly unstable.

To further study these equilibria, the dependency of WD_{min} on the amplitude and phase at inlet II is investigated. For 0.31 m $\leq A^{II}_{M_2} \leq$ 1.24 m and phases $|\phi^{II}_{M_2}| \geq 60°$ it is found that WD_{min} of stable equilibria occur at the entrances reaching the minimum water depth of 11.7 m. Therefore, in the following we focus on $|\phi^{II}_{M_2}| < 60°$, while $A^{II}_{M_2}$ is varied between 0.31 and 1.24 m. In Figure 5a, the depth of the watersheds is shown as a function of the amplitude and phase of the M_2 tide at inlet II. From this figure it follows that by increasing $A^{II}_{M_2}$ from 0.31 to 1.24 m and/or $\phi^{II}_{M_2}$ from −60° to 60° results in a shift of WD_{min} from a location closer to inlet I to a location closer to inlet II. The black line in the figure denotes the location where WD_{min} vanishes and, consequently, the double-inlet system reduces to two single-inlet systems.

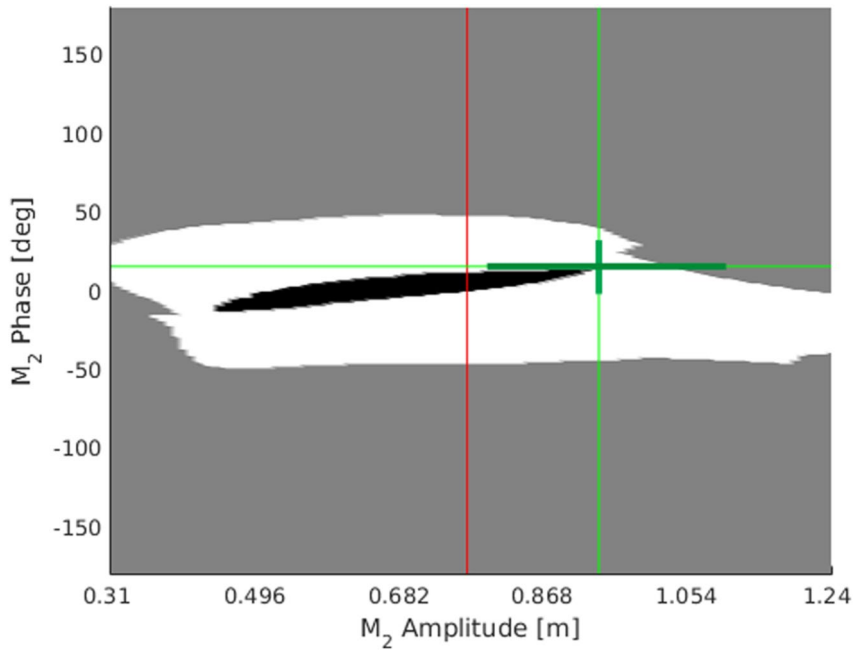

Figure 4. Number of morphodynamic equilibria as a function of amplitude (horizontal axis) and phase (vertical axis) of the forcing tidal constituent. Regions with no morphodynamic equilibria are shown in black, regions with one equilibrium in gray, and regions with two or more morphodynamic equilibria in white. The red and (dark) green lines correspond to the amplitudes and phases used in Figures 3d, 5b, and 5c.

In two regions in the $(A^{II}_{M_2}, \phi^{II}_{M_2})$-space, complex bifurcation structures occur, indicating that possibly multiple stable morphodynamic equilibria exist. To assess the number of equilibria, the bifurcation structure is carefully analyzed over two paths in parameter space, with one path characterized by a fixed amplitude and varying phase, and the second path by a fixed phase and varying amplitude.

The values of $\mathrm{WD}_{\mathrm{min}}$ for the first path in parameter space, that is, $A^{II}_{M_2} = 0.94$ m and $\phi^{II}_{M_2}$ in the range of 0°–30° is shown in Figure 5b. This figure shows that the number of morphodynamic equilibria depends sensitively on the phase angle. Similarly in Figure 5c, $\mathrm{WD}_{\mathrm{min}}$ is shown for M_2 amplitudes varied between 0.80 and 1.10 m, with the phase fixed at 15.5°. This figure illustrates that the number of morphodynamic equilibria also depends sensitively on the amplitude.

The vertical black lines in Figures 5b and 5c correspond to the same parameter values ($A^{II}_{M_2} = 0.94$ m, $\phi^{II}_{M_2} = 15.5°$). Hence, the equilibrium bed configurations denoted by $E1 - E4$, are the same in both figures. These bed profiles are shown in Figure 6. Equilibria $E1$ and $E3$ are linearly stable, whereas $E2$ and $E4$ are linearly unstable. Each equilibrium is characterized by a different balance between the various transport terms, contributing to a different, spatially uniform, and total sediment transport. These contributions, divided in two diffusive contributions and one total advective contribution (see Equation 10), and the total transport are shown in Figures 7a, 7c, and 7e, 7g, while Figures 7b, 7d, 7f, and 7h show the different contributions to the advective contribution. In all cases, the total transport is positive, indicating a net transport from inlet I to inlet II. These plots show that all transport mechanisms result in significant contributions to the total transport.

Moreover, Figure 8 indicates that the direction and magnitude of the total transport strongly depends on the forcing conditions at inlet II. Note the presence in the parameter space of a region in which the net sediment transport is negative, indicating a tidally-averaged total transport from inlet II to inlet I. Increasing $\phi^{II}_{M_2}$ results in a decrease of net transport from inlet II to inlet I on the left of the thin black lines, that indicate a zero transport, or an increase of net transport from inlet I to inlet II on the right of these lines.

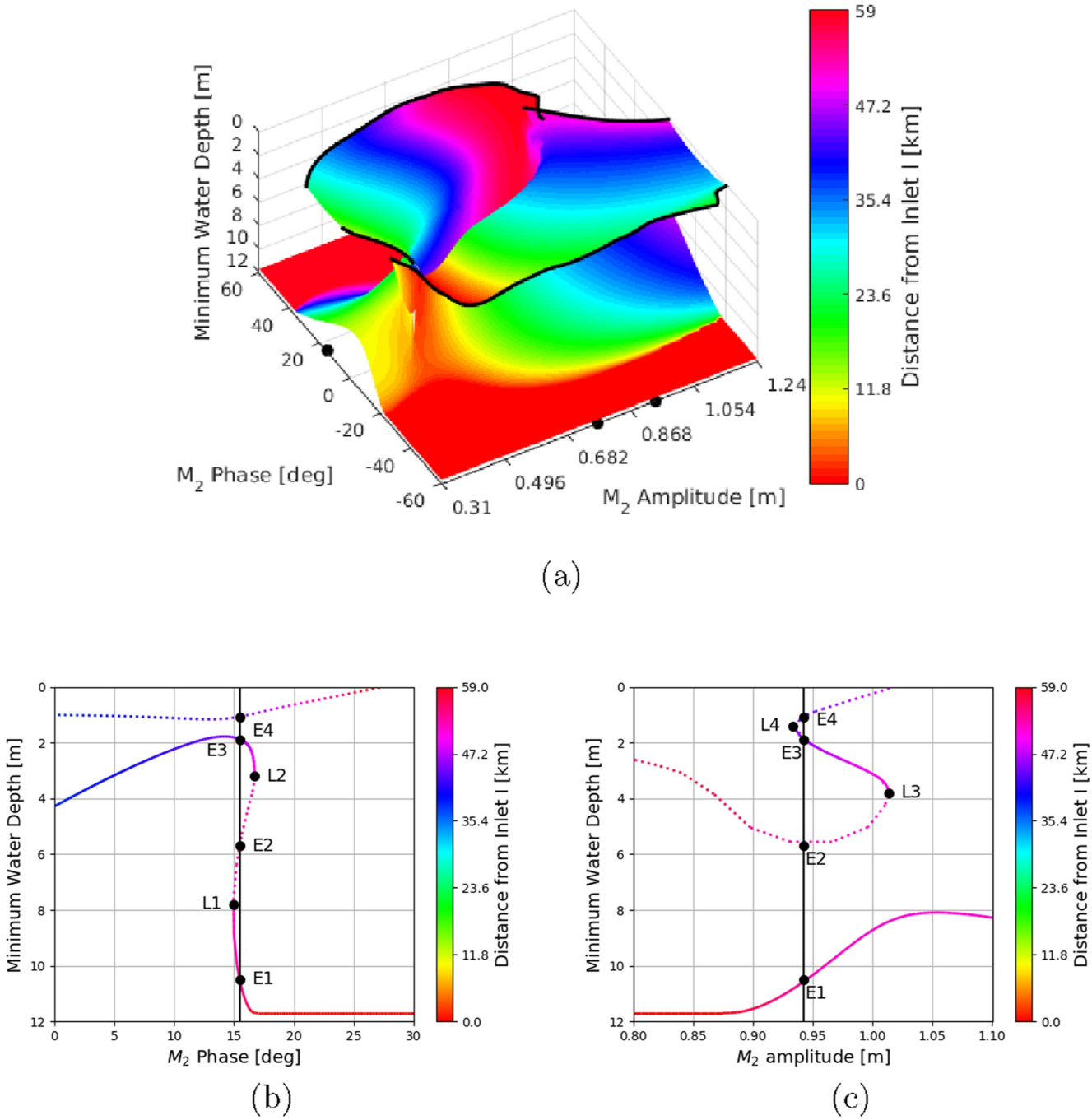

Figure 5. Morphodynamic equilibria for a constant-width inlet system with a M_2 tide. Panel (a) shows WD_{min} for the equilibrium configurations computed with $\phi^{II}_{M_2}$ in the range (−60°, 60°) and $A^{II}_{M_2}$ varying from 0.31 to 1.24 m. The black dots denote the parameter values used in Figures 3d, 5b, and 5c. Panel (b) shows WD_{min} of equilibria for $A^{II}_{M_2} = 0.94$ m and $\phi^{II}_{M_2}$ varying in the range (0°, 30°). Panel (c) shows the same information as in panel (b), but with $\phi^{II}_{M_2} = 15.5°$ and $A^{II}_{M_2}$ in the range (0.80 m and 1.10 m). The color indicates the location of the WD_{min}, with warmer colors closer to (one of) the entrance(s), and colder colors more toward the middle of the channel. Solid lines in panels (b) and (c) denote linearly stable equilibrium configurations, while dotted lines correspond to linearly unstable equilibrium configurations.

4.2. Constant-Width System Subjected to All Forcings

In this section, all hydrodynamic forcings are taken into account. They consist of M_2 and M_4 constituents prescribed at both inlets and a tidally-averaged water transport, prescribed at inlet *II*. The complete morphodynamic

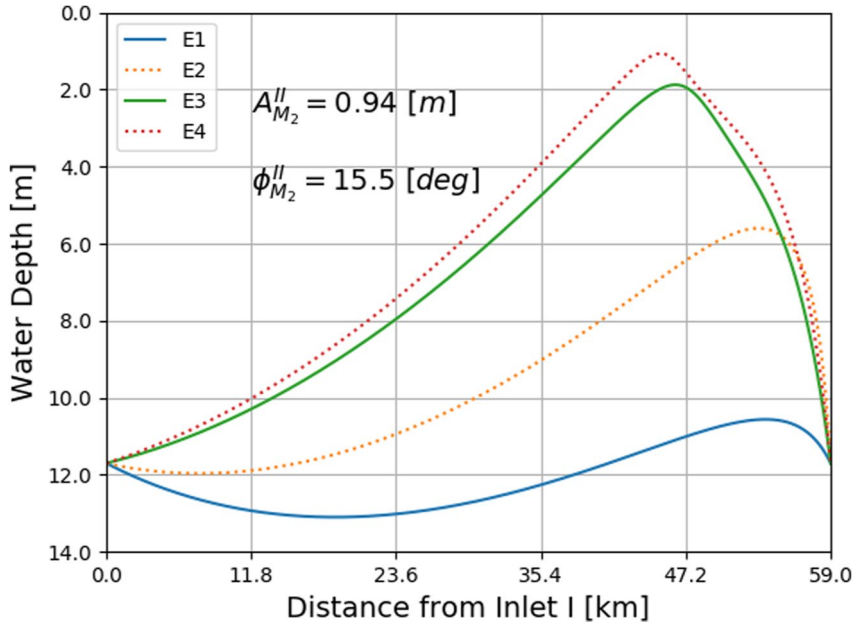

Figure 6. The bed profiles corresponding to the equilibrium configurations $E1$, $E2$, $E3$, and $E4$ indicated by black dots in Figures 5b and 5c.

equilibrium condition up to orders $O(\epsilon^2, \epsilon\gamma)$ has to be solved. It reads:

$$\frac{d}{dx}\left(<F^{00}_{\text{diff}}> + <F^{00}_{\text{topo}}> + <F^{20}_{\text{adv}}> + <F^{11}_{\text{adv}}>\right) = 0, \tag{28}$$

with the transport terms on the left-hand side given in Equations 20–22. All parameter values are taken from Table 1, except for the M_4 phase at inlet II, $\phi^{II}_{M_4}$, which is varied between $-180°$ and $180°$. Only linearly stable morphodynamic equilibria are discussed below.

The sensitivity of morphodynamic equilibria to $\phi^{II}_{M_4}$ is illustrated in Figure 9a, where the water depth is shown as a function of distance to inlet I (horizontal axis) and $\phi^{II}_{M_4}$ (vertical axis). The total sediment transport of the stable morphodynamic equilibria is shown in Figure 9b as a function of $\phi^{II}_{M_4}$, illustrating the sensitivity of both direction and magnitude of the total transport to $\phi^{II}_{M_4}$.

In Figure 9c, the equilibrium water depths are shown for some selected values of $\phi^{II}_{M_4}$. Focusing on $-121°$ (for the other phases, see Text S4 in Supporting Information S1), the total sediment transport, is split into its four main contributions in Figure 9d. The two diffusive contributions, $<F^{00}_{\text{diff}}>$ and $<F^{00}_{\text{topo}}>$, are only significant near inlet I. The sediment transport related to the internally-generated overtides, $<F^{20}_{\text{adv}}>$, is mostly directed from inlet II to inlet I, whereas the transport due to external overtides, $<F^{11}_{\text{adv}}>$, occurs in the largest part of the double-inlet system and is directed from inlet I to inlet II. The advective contributions can be further dissected in different components (see Text S4 in Supporting Information S1). It turns out that only two contributions dominate $<F^{20}_{\text{adv}}>$, namely the transport of tidally-averaged concentration by the tidally-averaged flow $<u^{10}><C^{00}>$ and the correlation of $u^{00}_{c1}C^{10}_{c1}$. Similarly, there are two main contributions to $<F^{11}_{\text{adv}}>$, that is, $u^{00}_{c1}C^{01}_{c1}$ and $u^{01}_{c2}C^{00}_{c2}$.

4.3. Varying-Width System Subjected to All Forcings

To illustrate the influence of width variations on the morphodynamic equilibria, the width is varied as,

$$B/B^I = 1 + \frac{c_0}{2\ \tanh(2.5)}\left[\tanh\left(\frac{0.75 - x/L}{0.1}\right) + \tanh\left(\frac{x/L - 0.25}{0.1}\right)\right], \tag{29}$$

where c_0 is a parameter that controls the width variation. This width distribution is chosen to be able to systematically vary the width when moving away from the entrances, a geometric feature often observed in tidal

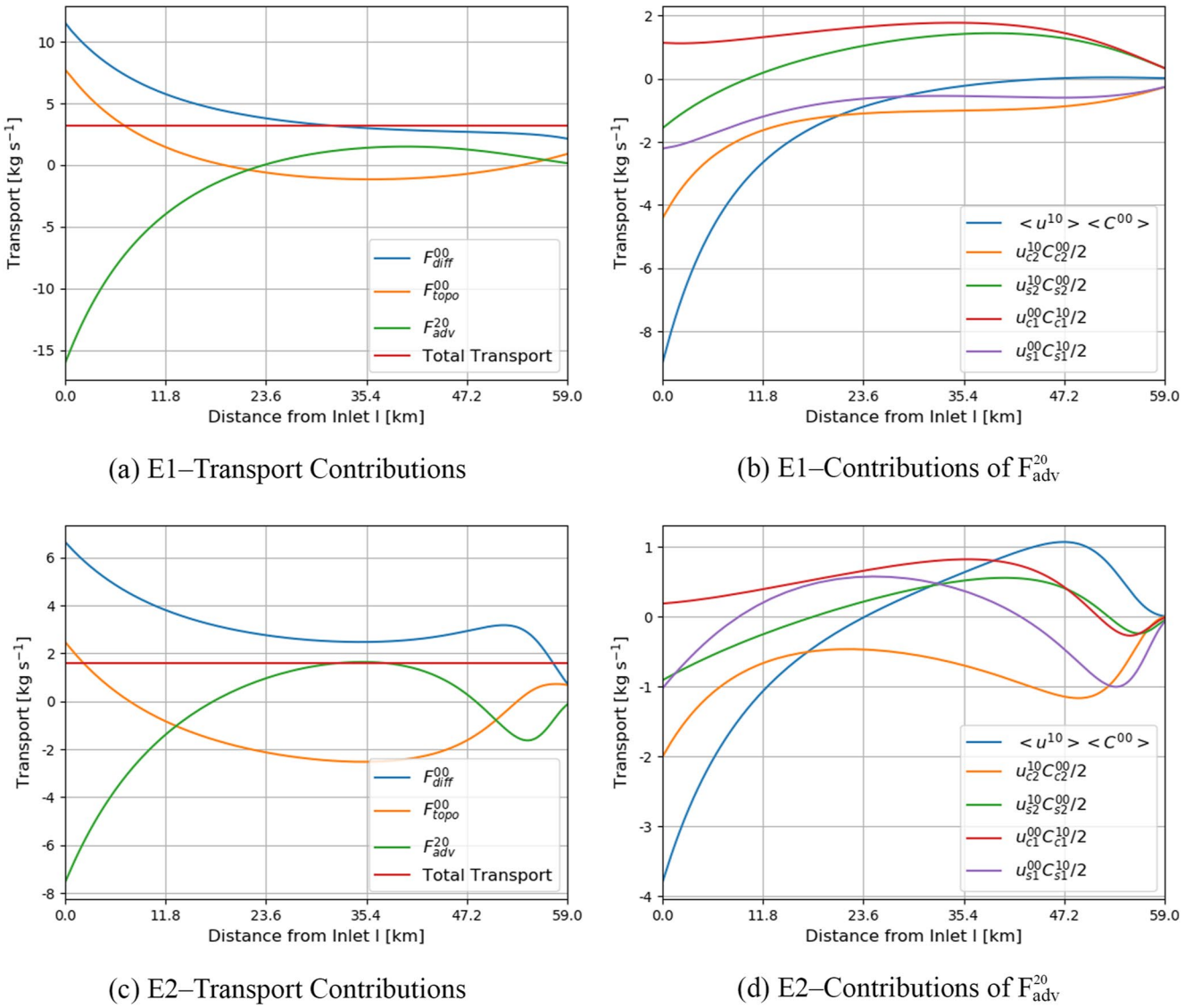

Figure 7. Panels (a, c, e, g) show the various transport contributions characterizing the equilibrium configurations *E*1, *E*2, *E*3, and *E*4 as a function of the location within the inlet system. Panels (b, d, f, h) depict the contributions to the advective transport for *E*1, *E*2, *E*3, and *E*4.

inlet systems. When $c_0 = 0$ the geometry reduces to the constant width-geometry used in the previous sections. Increasing (decreasing) c_0 results in a double-inlet system with a width that increases (decreases) toward the middle of the inlet system as shown in Figure 10a. The associated equilibrium water depths are shown in Figure 10b, while Figure 10c reports the equilibrium water depth as a function of c_0 (vertical axis) and of location in the double-inlet system (horizontal axis). Figure 10d shows the total sediment transport as a function of c_0. This transport is directed from inlet II to inlet I for a rectangular inlet system ($c_0 = 0$), and decreases for increasing width variation. If the width in the middle of the inlet system is approximately 50% larger than at the inlets, the total transport vanishes. For even larger width variations, the transport is directed from inlet I to inlet II.

The various contributions to the transport can again be split into its different contributions (see Text S4 in Supporting Information S1). For small enough c_0 (i.e., $c_0 < 0.5$), the magnitude of $< F^{20}_{adv} >$ is larger than that of $< F^{11}_{adv} >$. Since $< F^{20}_{adv} >$ is directed from inlet II to inlet I, the total transport is negative. When c_0 is increased, the relative importance of $< F^{11}_{adv} >$ increases, resulting in a total transport from inlet I to inlet II for large enough c_0.

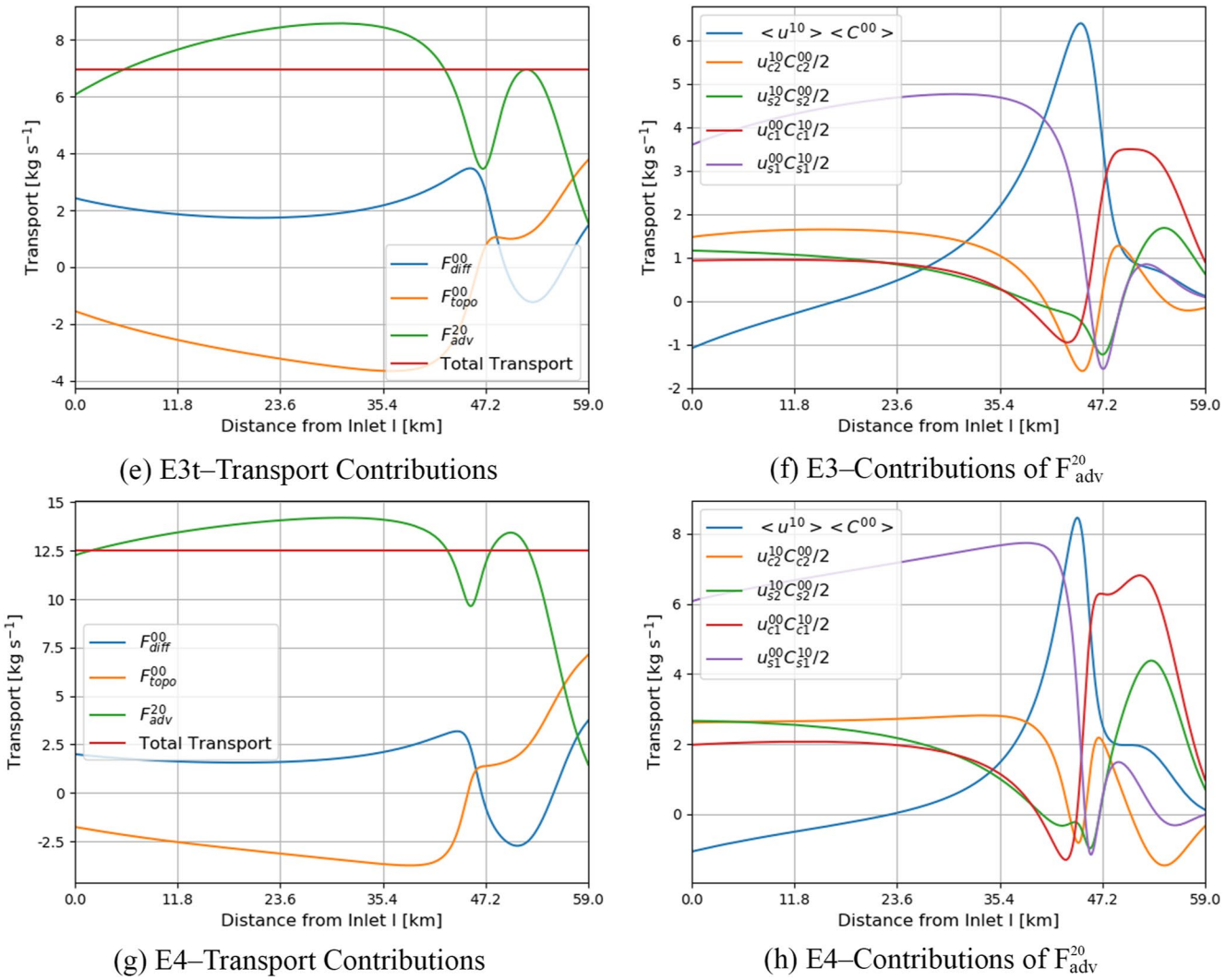

(e) E3t–Transport Contributions

(f) E3–Contributions of F^{20}_{adv}

(g) E4–Transport Contributions

(h) E4–Contributions of F^{20}_{adv}

Figure 7. *Continued.*

5. Discussion

5.1. Morphodynamic Equilibria

The results presented in Section 4 suggest that, the number and (linear) stability of morphodynamic equilibria in double-inlet systems depends sensitively on the forcing conditions and model geometry. For a rectangular geometry, with the water motion forced by one tidal constituent, the full bifurcation diagram indicates that for most parameter values, either one unique stable equilibrium or no morphodynamic equilibrium may exist in a system with the two inlets connected together. However, in a small part of the parameter space, more than one stable equilibrium was found.

Qualitatively, these observations concerning the number of morphodynamic equilibria and their stability are consistent with model results obtained using the modeling approach employed by van de Kreeke et al. (2008) and Brouwer et al. (2012). In these models, only the tidal inlets are morphodynamically active, while the prescribed bathymetry in the back-barrier basin is assumed uniform and constant in time. In particular, van de Kreeke et al. (2008) investigated the influence of a topographic high on the existence and stability of morphodynamic equilibria. They found that, depending on the height of this topographic high, no equilibrium, one unique stable equilibrium or two stable equilibria could exist. On the other hand, Brouwer et al. (2012) showed that the existence of these equilibria depends sensitively on the amplitude and phase of the M_2 tide at the seaward side

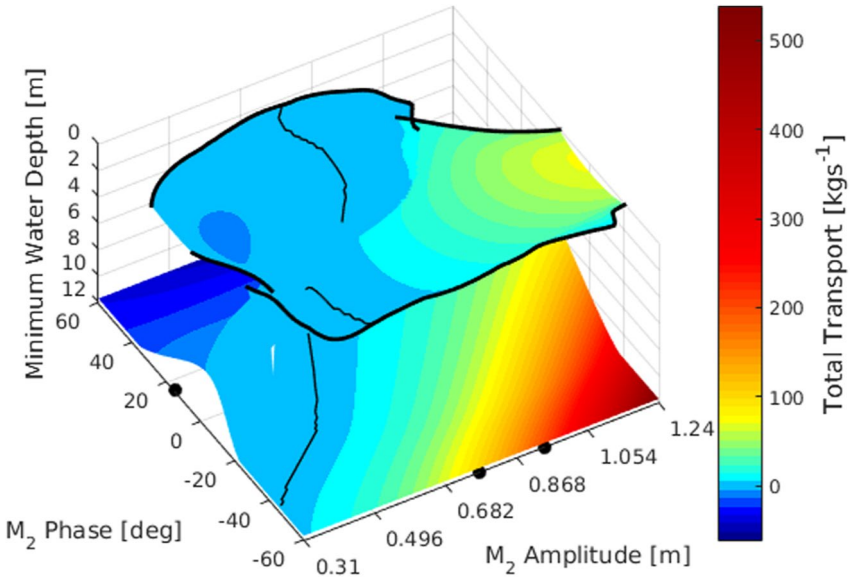

Figure 8. Total transport characterizing the equilibrium bed profiles. The thin black lines indicate equilibria with a vanishing tidally-averaged total transport. The black dots denote the parameter values used in Figures 3d, 5b, and 5c.

of the tidal inlets. Even though these results seem to confirm the findings of Section 4 (i.e., sensitivity of the number and the stability of morphodynamic equilibria to geometry and forcing), it should be realized that the model formulations are quite different and hence that results obtained with the different approaches are difficult to compare.

5.2. Comparison With Results of a Complex Numerical Model

In this section, we compare the cross-sectionally averaged water motion obtained with the present model, with the results of a state-of-the-art process-based numerical model, and the modeled equilibrium bathymetry with that observed in the field. The numerical model used to calculate the water motion is the General Estuarine Transport Model (GETM), a three-dimensional model that solves the hydrodynamic equations using a finite difference approach. Effects of drying and flooding are included. For an extensive discussion of the model features and the application site we refer the reader to Duran-Matute et al. (2014). The planform geometry and the bathymetry of the double-inlet tidal system were obtained from field observations and are shown in Figure 2a. In this figure, the Marsdiep inlet is denoted as inlet I and the Vlie inlet as inlet II. The Wadden islands and mainland are colored in white, whereas the water depth is shown in color scale.

The width distribution as a function of distance to inlet I to be used in the present model were obtained by smoothly connecting points with a water depth of 1 m indicated with triangles in Figure 2a. Using these lines, the basin centerline was constructed. This line was parameterized by the spatial coordinate x, which starts at inlet I ($x = 0$) and ends at inlet II ($x = 59$ km). The width as a function of x is defined as the length of the lines perpendicular to the basin centerline. Furthermore, the depth is obtained by averaging the observed depths over the width.

The resulting width profile is shown in Figure 11a. The double-inlet system is characterized by a small width near the seaward sides, but also around 31 km. At this location, the width is restricted by the presence of the tidal divide between the Eierlandse gat and the Marsdiep-Vlie system on the northern side, and the mainland in the south. This width profile has then been used to compute the values of the width-averaged depth at both entrances, as well as of amplitudes and phases of the tidal constituents (see Table 1).

Figure 11b shows the width-averaged amplitudes of the M_2 and M_4 tidal constituents obtained with the present equilibrium model and computed from the GETM model. The overall trend appears to be well captured. Furthermore, there is a good correspondence with the amplitudes computed with the present model and those presented in Ridderinkhof (1988) and Hepkema et al. (2018), in which the hydrodynamics of the Marsdiep-Vlie system was investigated through cross-sectionally averaged models.

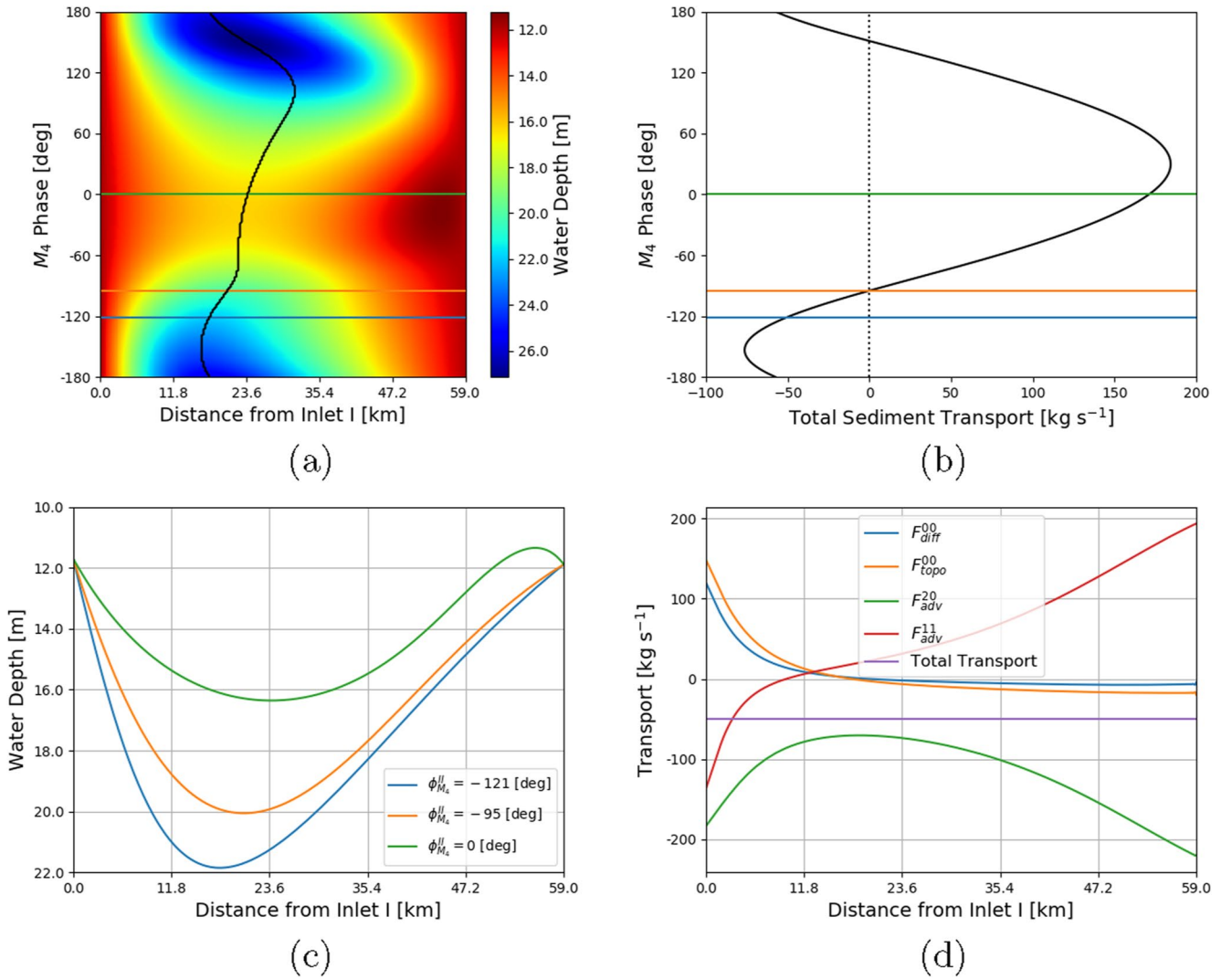

Figure 9. Stable morphodynamic equilibria for varying $\phi^{II}_{M_4}$ and including all forcing terms. Panel (a) shows the bed profiles of stable morphodynamic equilibria, with warmer (colder) colors indicating smaller (larger) water depths. The black line indicates the location of WD_{max}. Panel (b) shows the total sediment transport of the morphodynamic equilibria. Panel (c) reports equilibrium bed profiles for some selected values of $\phi^{II}_{M_4}$, namely $\phi^{II}_{M_4} = 0°, -95°$, and $-121°$, respectively. The water depths and total transports for these phases are indicated by the blue, orange and green line in Figures 9a and 9b. The associated transports obtained with $\phi^{II}_{M_4} = -121°$ (the default value for $\phi^{II}_{M_4}$, see Table 1) are shown in panel (d). Total transport, $<F^{00}_{diff}>$, $<F^{00}_{topo}>$, $<F^{20}_{adv}>$, and $<F^{11}_{adv}>$ are indicated by the purple, blue, orange, green, and red, respectively.

The equilibrium water depth is shown in Figure 11c. There is a good qualitative comparison between the observed and modeled equilibrium water depth. In particular, the dramatic depth increase when moving from inlet I a few kilometers into the basin is well-captured. When moving toward inlet II, it is observed that the distribution of the depth variations is well-captured, but the water depth in the model is typically overestimated with respect to observed data.In Figure 11d, the various transport contributions in morphodynamic equilibrium are shown. It is observed that, the total sediment transport is from inlet I to inlet II. In the first few kilometers, the dominant transport contribution is given by topographic diffusion and is directed from inlet I to II, whereas all other contributions are in the opposite direction. The topographic diffusive sediment transport contribution is directly related to the relatively fast increase of the water depth when moving into the basin. When moving further into the basin, the water depth decreases again and topographic diffusion changes sign. However, there is still a net transport toward inlet II due to internally generated advection and diffusion that changed sign as well. Moving even further toward inlet II ($x > 24$ km), the transport due to the externally-prescribed overtide dominates, resulting in a net transport in the direction of inlet II. The direction of transport at inlet I, the Marsdiep Inlet, is in agreement with

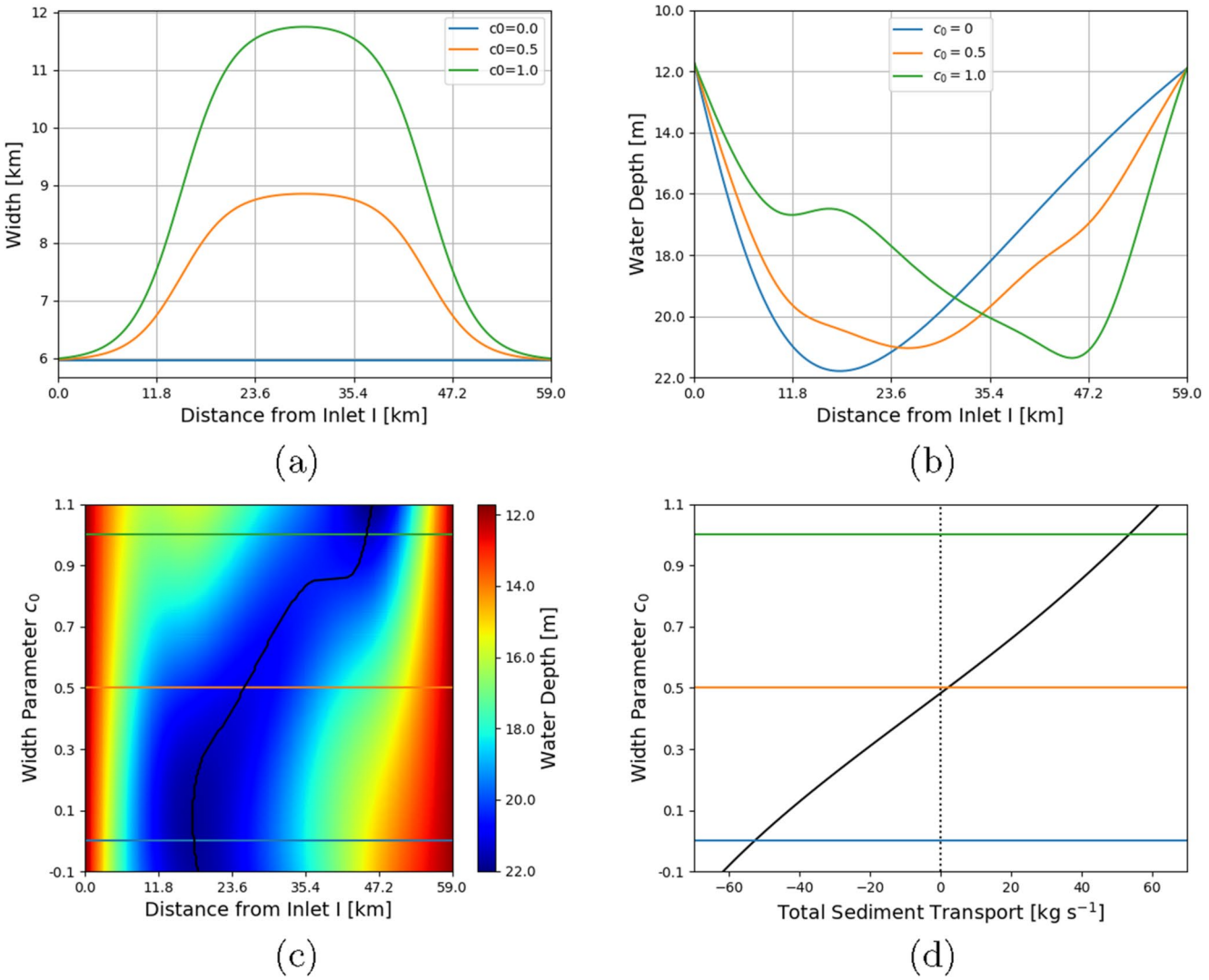

Figure 10. Stable morphodynamic equilibria obtained for different width distributions of the double-inlet system, including all forcings. Panel (a) shows the width distributions for some selected values of the width parameter c_0 (0, 0.5, and 1). Panel (b) reports the corresponding bed profile. Panel (c) shows the stable equilibrium bed profiles obtained for c_0 varying from −0.1 to 1.1. Panel (d) shows the total sediment transport of stable equilibria for the same variations of c_0.

the transport direction found in Sassi et al. (2015). In our model setup, this directly implies that in the second inlet, the Vlie, sediment should be exported. In Sassi et al. (2015), the median value of the sediment transport at the Vlie is close to zero, with both import and export found, depending on the specific forcing conditions. However, in the model setup of Sassi et al. (2015), the Wadden Sea is modeled as a multiple-inlet system, allowing for sediment transport over watersheds to adjacent basins that are not taken into account in the model schematization used in this paper.

Even though the main characteristics of the water motion (from a refined numerical model), and the main bathymetric features (from observations), are reproduced qualitatively well, there are still some differences. The main differences concerning the hydrodynamic quantities are found in regions with extensive tidal flats and multiple channels. In this study, variations in flow conditions over the cross-sectional area are not explicitly taken into account. It is possible to include these effects by modeling parametrically the effects of mass storage and momentum sinks (Friedrichs & Aubrey, 1994; Hepkema et al., 2018). However, to capture these effects dynamically, the existence and stability of morphodynamic equilibria in a two-dimensional (depth-averaged) model have to be studied. The results obtained with the cross-sectionally averaged model are essential input for models in which the above effects are incorporated explicitly (Boelens et al., 2021; Dijkstra et al., 2014). Furthermore, in reality

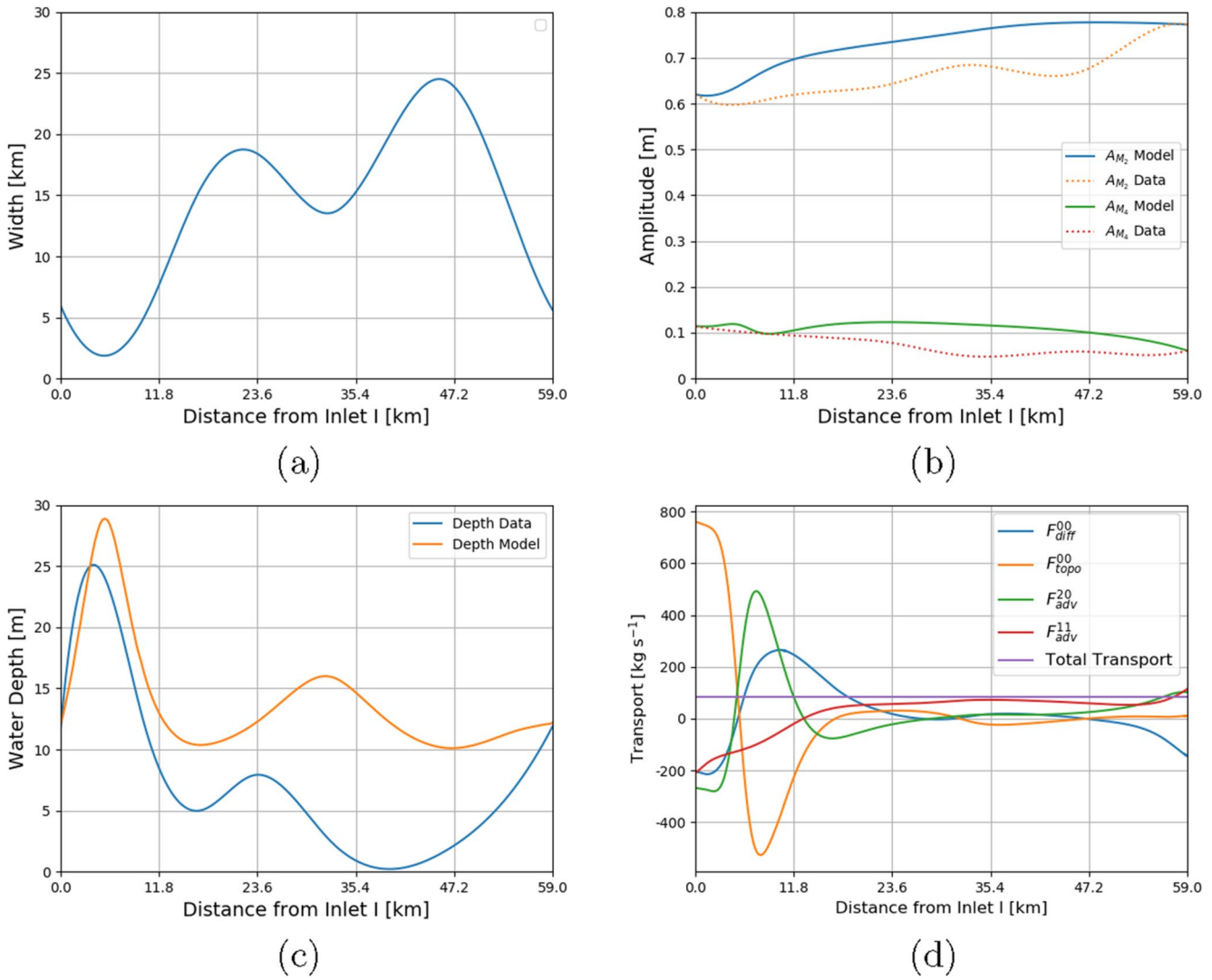

Figure 11. Comparison between the stable morphodynamic equilibria predicted by the present model, the real bathymetric data and the water motion obtained with GETM. The width of the double-inlet system is shown in panel (a). The amplitude of the M_2 and M_4 tides obtained from the high-complexity numerical model and the present model are compared in panel (b), while the observed and computed bed profile are compared in panel (c). Panel (d) displays the various sediment transport contributions, together with the total sediment transport (indicated with the purple line) which is directed from inlet I to inlet II.

water and sediment are transported over the watersheds to adjacent tidal inlet systems (Duran-Matute et al., 2014; Sassi et al., 2015). These transport processes can only be captured by extending the present model to a morphodynamic model for multiple inlet systems (Reef et al., 2020; Roos et al., 2013).

Also, the width-averaged equilibrium bathymetry obtained with the present model exhibits the largest deviations with respect to the observed data in regions with extensive tidal flats. There, the effects of wind and waves can play an important role (de Swart & Zimmerman, 2009; Marciano et al., 2005). Furthermore, the possible import of sediment due to littoral drift along the coast of the sea is neglected in the present study. This transport mechanism was shown to be important by van de Kreeke et al. (2008) and Roos et al. (2013).

6. Conclusions

An idealized model has been developed to systematically investigate the existence of cross-sectionally averaged morphodynamic equilibria in double-inlet systems. A morphodynamic equilibrium is defined by the condition for which the bottom does not evolve anymore, requiring the tidally-averaged sediment transport to be spatially

uniform. The model consists of the cross-sectionally averaged shallow water equations, a width-averaged and depth-integrated advection-diffusion equation for the suspended sediment dynamics and a width-averaged bed evolution equation.

The morphodynamic equilibria have been computed by using a so-called *bifurcation method*. This approach allows to obtain the equilibrium bed profiles (and associated water surface elevation, velocity and concentration fields) directly for given values of the relevant parameters, of the tidal forcing constituents, of the water depth at the seaward boundaries and the system geometry, without resorting to time-integration techniques.

Considering a double-inlet system with a constant width and forced by a M_2 tidal constituent at the seaward boundaries, it was shown that, depending on the prescribed M_2 amplitudes and phases, no equilibrium, one equilibrium or more than one morphodynamic equilibrium configurations exist. In the absence of a morphodynamic equilibrium, the water depth vanishes somewhere within the tidal basin and the double-inlet system reduces to two uncoupled single-inlet systems. In case of multiple morphodynamic equilibria, most often two equilibrium solutions are found, one linearly stable and the other one linearly unstable. However, for very specific regions of the parameter space, more than one stable equilibrium can be found, with typically one equilibrium having a much smaller minimum water depth than the other. When only one morphodynamic equilibrium was found, the equilibrium was always linearly stable.

The location of the watershed, the local depth at the watershed, and the total sediment transport are used to characterize the morphodynamic equilibria, since these properties are sensitive to changes in tidal forcing. Typically, the watershed tends to get closer to the inlet with a larger tidal amplitude. The total transport is usually directed from the inlet with the largest tidal amplitude to the one with the smallest tidal amplitude, with a weak dependency on the phase difference between the tidal forcing at the two inlets.

The model results have been compared with observations by forcing the system with the first two tidal constituents and considering a tidally-averaged water velocity at one of the inlets. Furthermore, the observed width distribution along the basin has to be prescribed in the model. Taking parameter values representative of the Marsdiep-Vlie system one stable morphodynamic equilibrium was found. To assess the robustness of this equilibrium, the phase of the M_4 tide at one of the inlets and the width profile of the double-inlet system were systematically varied. The resulting bathymetry and direction of sediment transport were found to strongly depend on these parameters. This finding suggests that information concerning morphodynamic equilibria for double-inlet systems with characteristics different from those of the Marsdiep-Vlie system can only be obtained by dedicated numerical experiments to explore the parameter space.

Taking the large-scale width variations observed in the Marsdiep-Vlie system into account, the main characteristics of the observed width-averaged bathymetry in this double-inlet system were qualitatively reproduced. The large water depth near the Texel Island was found in the model results, as well as two shallower regions, divided by a deeper part, when moving toward the Vlie inlet. Even though the residual water transport is directed from the Vlie inlet to the Marsdiep inlet, the model predicts a sediment transport in the opposite direction. This transport from the Marsdiep to the Vlie system is also found in much more refined numerical models. Furthermore, the order of magnitude of this transport, predicted by the numerical model, is well-reproduced by the model presented in this paper.

Conflict of Interest

The authors declare no conflicts of interest relevant to this study.

Acknowledgments
The authors thank Matias Duran-Matute for making the data of the GETM model, used in Duran-Matute et al. (2014) available to us. The authors thank Pieter Roos, Huib de Swart, and three anonymous reviewers for their comments on this paper. The authors also thank USGS/ESA for granting permission to use Figure 1. This article is financially supported by the China Scholarship Council (nr. 201706890036).

References

Alnæs, M., Blechta, J., Hake, J., Johansson, A., Kehlet, B., Logg, A., et al. (2015). The FEniCS project version 1.5. *Archive of Numerical Software*, *3*(100).

Boelens, T., Qi, T., Schuttelaars, H., & De Mulder, T. (2021). Morphodynamic equilibria in short tidal basins using a 2DH exploratory model. *Journal of Geophysical Research: Earth Surface*, *126*(3). https://doi.org/10.1029/2020JF005555

Bolla Pittaluga, M., Tambroni, N., Canestrelli, A., Slingerland, R., Lanzoni, S., & Seminara, G. (2014). Where river and tide meet: The morphodynamic equilibrium of alluvial estuaries. *Journal of Geophysical Research: Earth Surface*, *120*(1), 75–94. https://doi.org/10.1002/2014JF003233

Brenner, S. C., Scott, L. R. (2002). *The mathematical theory of finite element methods* (2nd ed.). Springer.

Brouwer, R. L., van de Kreeke, J., & Schuttelaars, H. M. (2012). Entrance/exit losses and cross-sectional stability of double inlet systems. Estuarine. *Coastal and Shelf Science*, *107*, 69–80. https://doi.org/10.1016/j.ecss.2012.04.033

Crisfield, M. A. (1981). A fast incremental/iterative solution procedure that handles snap through. *Computers & Structures*, *13*, 55–62. https://doi.org/10.1016/0045-7949(81)90108-5

Csanady, G. T. (1982). *Circulation in the coastal ocean*. Reidel.

Dastgheib, A., Roelvink, J. A., & Wang, Z. B. (2008). Long-term process-based morphological modeling of the Marsdiep tidal basin. *Marine Geology*, *256*, 90–100. https://doi.org/10.1016/j.margeo.2008.10.003

de Swart, H. E., & Volp, N. D. (2012). The effect of hypsometry on the morphodynamical stability of single and multiple tidal inlet systems. *Journal of Sea Research*, *74*, 35–44. https://doi.org/10.1016/j.seares.2012.05.008

de Swart, H. E., & Zimmerman, J. T. F. (2009). Morphodynamics of tidal inlet systems. *Annual Review of Fluid Mechanics*, *41*, 203–229. https://doi.org/10.1146/annurev.fluid.010908.165159

Dijkstra, H. A., Wubs, F. W., Cliffe, A. K., Doedel, E., Dragomirescu, I. F., Eckhardt, B., et al. (2014). Numerical bifurcation methods and their application to fluid dynamics: Analysis beyond simulation. *Communications in Computational Physics*, *15*, 1–45. https://doi.org/10.4208/cicp.240912.180613a

Duran-Matute, M., Gerkema, T., de Boer, G. J., Nauw, J. J., & Grawe, U. (2014). Residual circulation and freshwater transport in the Dutch Wadden Sea: A numerical modelling study. *Ocean Science*, *10*, 611–632. https://doi.org/10.5194/os-10-611-2014

Dyer, K. R. (1986). *Coastal and estuarine sediment transport* (p. 342). John Wiley and Sons.

Escoffier, F. (1940). The stability of tidal inlets. *Shore and Beach*, *8*, 114–115.

Friedrichs, C., & Aubrey, D. (1994). Tidal propagation in strongly convergent channels. *Journal of Geophysical Research*, *99*, 3321–3336. https://doi.org/10.1029/93jc03219

Glaeser, D. J. (1978). Global distribution of barrier islands in terms of tectonic setting. *Journal of Geophysical Research*, *86*, 283–297. https://doi.org/10.1086/649691

Hayes, M. O. (1979). In S. P. Leatherman (Ed.), *Barrier island morphology as a function of tidal and wave regime*. Academic Press.

Hepkema, T., de Swart, H., Zagaris, A., & Duran–Matute, M. (2018). Sensitivity of tidal characteristics in double inlet systems to momentum dissipation on tidal flats: A perturbation analysis. *Ocean Dynamics*, *68*(4–5), 439–455. https://doi.org/10.1007/s10236-018-1142-z

Krol, M. (1991). On the averaging method in nearly time periodic advection-diffusion problems. *SIAM Journal on Applied Mathematics*, *51*, 1622–1637. https://doi.org/10.1137/0151083

Lanzoni, S., & Seminara, G. (2002). Long-term evolution and morphodynamic equilibrium of tidal channels. *Journal of Geophysical Research*, *107*, 1–13. https://doi.org/10.1029/2000jc000468

Lorentz, H. (1922). *Het in rekening brengen van den weerstand bij schommelende vloeistofbewegingen* (Vol. 695). De Ingenieur.

Marciano, R., Wang, Z., Hibma, A., De Vriend, H., & Defina, A. (2005). Modeling of channel patterns in short tidal basins. *Journal of Geophysical Research*, *110*(1). https://doi.org/10.1029/2003jf000092

McBride, R. A., Byrnes, M. R., & Hiland, M. W. (1995). Geomorphic response-type model for barrier coastlines: A regional perspective. *Marine Geology*, *126*, 143–159. https://doi.org/10.1016/0025-3227(95)00070-f

Meerman, C. J., Schuttelaars, H. M., & Rottschafer, V. (2019). Influence of geometrical variations on morphodynamic equilibria for single inlet systems. *Ocean Dynamics*, *69*(221–238), 2. https://doi.org/10.1007/s10236-018-1236-7

Mulhern, J., Johnson, C., & Martin, J. (2017). Is barrier island morphology a function of tidal and wave regime? *Marine Geology*, *387*, 74–84. https://doi.org/10.1016/j.margeo.2017.02.016

Oost, A. P., Hoekstra, P., Wiersma, A., Flemming, B., Lammerts, E. J., Pejrup, M., et al. (2012). Barrier island management: Lessons from the past and directions for the future. *Ocean & Coastal Management*, *68*, 18–38. https://doi.org/10.1016/j.ocecoaman.2012.07.010

Pacheco, A., Vila-Concejo, A., Ferreira, O., & Dias, J. A. (2008). Assessment of tidal inlet evolution and stability using sediment budget computations and hydraulic parameter analysis. *Marine Geology*, *247*, 104–127. https://doi.org/10.1016/j.margeo.2007.07.003

Reef, K., Roos, P., Schuttelaars, H., & Hulscher, S. (2020). Influence of back-barrier basin geometry on multiple tidal inlet systems: The roles of resonance and bottom friction. *Journal of Geophysical Research: Earth Surface*, *125*(3). https://doi.org/10.1029/2019jf005261

Ridderinkhof, H. (1988). Tidal and residual flows in the western Dutch Wadden Sea II: An analytical model to study the constant flow between connected tidal basins. *Netherlands Journal of Sea Research*, *22*, 185–198. https://doi.org/10.1016/0077-7579(88)90022-1

Roos, P. C., & Schuttelaars, H. M. (2015). Resonance properties of tidal channels with multiple retention basins: Role of adjacent sea. *Ocean Dynamics*, *65*(3), 311–324. https://doi.org/10.1007/s10236-015-0809-y

Roos, P. C., Schuttelaars, H. M., & Brouwer, R. L. (2013). Observations of barrier island length explained using an exploratory morphodynamic model. *Geophysical Research Letters*, *40*, 4338–4343. https://doi.org/10.1002/grl.50843

Salles, P., Voulgaris, G., & Aubrey, D. G. (2005). Contribution of nonlinear mechanisms in the persistence of multiple tidal inlet systems. Estuarine. *Coastal and Shelf Science*, *65*, 475–491. https://doi.org/10.1016/j.ecss.2005.06.018

Sanders, J. A., & Verhulst, F. (1985). *Averaging methods in nonlinear dynamical systems*. Spring-Verlag.

Sassi, M., Duran-Matute, M., van Kessel, T., & Gerkema, T. (2015). Variability of residual fluxes of suspended sediment in a multiple tidal-inlet system: The Dutch Wadden Sea. *Ocean Dynamics*, *65*(9–10), 1321–1333. https://doi.org/10.1007/s10236-015-0866-2

Schuttelaars, H. M., & de Swart, H. E. (1996). An idealized long-term morphodynamic model of a tidal embayment. *European Journal of Mechanics - B: Fluids*, *15*, 55–80.

Schuttelaars, H. M., & de Swart, H. E. (2000). Multiple morphodynamic equilibria in tidal embayments. *Journal of Geophysical Research*, *105*, 105–124. https://doi.org/10.1029/2000jc900110

Seminara, G., Bolla Pittaluga, M., Tambroni, N., & Garotta, V. (2005). Open problems modelling the long-term morphodynamic evolution of Venice lagoon. In C. A. Fletcher, & T. Spencer (Eds.), *Flooding and environmental challenges for Venice and its lagoon: State of knowledge* (pp. 369–378). Cambridge University Press.

Seydel, R. (1994). *Practical bifurcation and stability analysis*. Springer Verlag.

Stutz, M. L., & Pilkey, O. H. (2011). Open-ocean barrier islands: Global influence of climatic oceanographic, and depositional settings. *Journal of Coastal Research*, *27*, 207–222. https://doi.org/10.2112/09-1190.1

Tambroni, N., & Seminara, G. (2006). Are inlets responsible for the morphological degradation of Venice lagoon? *Journal of Geophysical Research*, *111*(3). https://doi.org/10.1029/2005jf000334

ter Brake, M. C., & Schuttelaars, H. M. (2010). Modeling equilibrium bed profiles of short tidal embayment. On the effect of the vertical distribution of suspended sediment and the influence of the boundary conditions. *Ocean Dynamics*, *60*, 183–204. https://doi.org/10.1007/s10236-009-0232-3

ter Brake, M. C., & Schuttelaars, H. M. (2011). Channel and shoal development in a short tidal embayment: An idealized model study. *Journal of Fluid Mechanics*, *677*, 503–529. https://doi.org/10.1017/jfm.2011.97

van de Kreeke, J. (1985). Stability of tidal inlets-Pass Cavallo, Texas. Estuarine. *Coastal and Shelf Science*, *21*, 33–43. https://doi.org/10.1016/0272-7714(85)90004-6

van de Kreeke, J. (1990a). Can multiple tidal inlets be stable? Estuarine. *Coastal and Shelf Science*, *30*, 261–273. https://doi.org/10.1016/0272-7714(90)90051-r

van de Kreeke, J. (1990b). Stability analysis of a two-inlet bay system. *Coastal Engineering*, *14*, 481–497. https://doi.org/10.1016/0378-3839(90)90031-q

van de Kreeke, J., Brouwer, R. L., Zitman, T. J., & Schuttelaars, H. M. (2008). The effect of a topographic high on the morphodynamical stability of a two inlet bay system. *Coastal Engineering*, *55*, 319–332. https://doi.org/10.1016/j.coastaleng.2007.11.010

van der Spek, A. J. F. (1997). Tidal asymmetry and long-term evolution of Holocene tidal basins in the Netherlands, simulation of paleotides in the Scheldt estuaries. *Marine Geology*, *141*, 71–90. https://doi.org/10.1016/s0025-3227(97)00064-9

Zimmerman, J. T. F. (1992). On the Lorentz linearization of a nonlinearly damped tidal Helmholtz oscillator. *Proceedings KNAW*, *95*, 127–145.